

*A CO J = 2→1 Study of the Outflow Sources
GL 490 and NGC 7538 IRS 9*

Jason Walter Schella

*A thesis presented to the Department of
Astronomy, St. Mary's University, in partial
fulfillment of the Master of Science degree.*

© 1991 Jason W. Schella



National Library
of Canada

Bibliothèque nationale
du Canada

Canadian Theses Service Service des thèses canadiennes

Ottawa, Canada
K1A 0N4

The author has granted an irrevocable non-exclusive licence allowing the National Library of Canada to reproduce, loan, distribute or sell copies of his/her thesis by any means and in any form or format, making this thesis available to interested persons.

The author retains ownership of the copyright in his/her thesis. Neither the thesis nor substantial extracts from it may be printed or otherwise reproduced without his/her permission.

L'auteur a accordé une licence irrévocable et non exclusive permettant à la Bibliothèque nationale du Canada de reproduire, prêter, distribuer ou vendre des copies de sa thèse de quelque manière et sous quelque forme que ce soit pour mettre des exemplaires de cette thèse à la disposition des personnes intéressées.

L'auteur conserve la propriété du droit d'auteur qui protège sa thèse. Ni la thèse ni des extraits substantiels de celle-ci ne doivent être imprimés ou autrement reproduits sans son autorisation.

ISBN 0-315-67031-2

Canada

Acknowledgements

I would like to thank everyone in the Astronomy Department at Saint Mary's for their support and understanding during the past 2.5 years. Dr. George Mitchell, whom I admire a great deal, has been very patient and helpful with my thesis project. Thank you for suggesting this extremely interesting topic. I would like to thank Dr. Gary Welch and Dr. David Turner for helping me in my course work and encouraging me in my studies. I wish to express my appreciation to Dr. Cameron Reed for being on the defense committee. Thanks to Dr. Tatsuhiko I. Hasegawa for his insightful suggestions for my thesis. I enjoyed our many chats.

I would also like to thank my fellow classmates Virginia MacSwain, Siow Wang Lee, and Jeremy Beckett for their help and their patience in putting up with me. They made my stay at Saint Mary's more enjoyable. I wish them the very best in the future. Special thanks go to Dr. Randall Brooks for his support of all the graduate students. He is a very understanding and caring person with a bit of an odd sense of humor.

Finally, and most importantly, I wish to thank my family for the support, encouragement, and understanding. At times I was probably difficult to get along with. I couldn't have made it without them.

Thank God I made it.

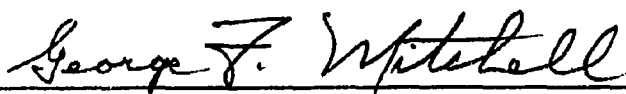
ABSTRACT

This thesis presents new detailed ^{12}CO and ^{13}CO observations, using 21" resolution, around the two luminous infrared sources GL 490 and NGC 7538 IRS 9. Observations show strong evidence for bipolarity of the high-velocity outflows surrounding these two objects. There is little doubt that the IR sources discussed here are the central driving objects behind the outflows.

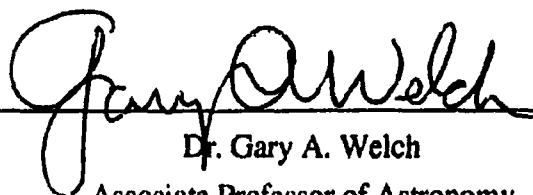
Spectra of the two isotopic forms, ^{12}CO and ^{13}CO , allow us to calculate the optical depth as well as the mass and other important physical properties of the two high-velocity outflows. Calculations of optical depth indicate that ^{12}CO $J = 2 \rightarrow 1$ emission is optically thick in the inner wings and optically thin in the outer wings. The total outflow masses were determined to be 9 M_{\odot} for GL 490 and 50 M_{\odot} for NGC 7538 IRS 9. The calculated mechanical luminosities of the outflows are much smaller than the stellar luminosities of the respective sources which is consistent with radiation pressure being the driving mechanism. The calculated force required to accelerate the molecular outflow is, however, much larger than the force that could be exerted on the gas if every photon emitted by the central object were absorbed. Unless thermal re-radiation is incorporated these molecular outflows must be driven by some mechanism other than radiation pressure.

The dynamical timescales of the outflows are fairly similar to each other: $\sim 10,000$ years for GL 490 and $\sim 30,000$ years for NGC 7538 IRS 9, implying that they are at similar stages in their evolution. Mass loss rates were calculated by dividing total outflow mass by the dynamical timescale and were found to be $1.7 \times 10^{-3} M_{\odot}/\text{yr}$ for NGC 7538 IRS 9 and $\sim 6 \times 10^{-4} M_{\odot}/\text{yr}$ for GL 490. Our observations imply that much of the emission arises from swept-up material which is possibly the result of the interaction of a collimated wind and the ambient molecular cloud.

The Examining Committee



Dr. George F. Mitchell
Professor of Astronomy
St. Mary's University
(Thesis Supervisor)



Dr. Gary A. Welch
Associate Professor of Astronomy
St. Mary's University



Dr. B. Cameron Reed
Associate Professor of Physics
St. Mary's University

TABLE OF CONTENTS

Acknowledgements	i
Abstract	ii
The Examining Committee	iv
List of Tables	vi
List of Figures	vii
I. Introduction	
a) Star Forming Clouds	2
b) Evidence for Molecular Outflows	3
c) GL 490 Background	13
d) NGC 7538 IRS9 Background	15
II. Observations and Data Analysis	
a) Equipment Used	18
b) Reduction Programs	24
c) Derivations of Important Physical Parameters	25
d) Uncertainties	31
III. Results	
a) GL 490	33
b) NGC 7538 IRS9	46
IV. References	65
Appendix A	68
Appendix B	72
Curriculum Vitae	83

LIST OF TABLES

Table 1.	List of Observations _____	19
Table 2.	Velocity Ranges for ^{12}CO Profiles in GL 490 _____	37
Table 3.	Velocity Ranges for ^{12}CO Profiles in NGC 7538 IRS 9 _____	49
Table 4.	Dynamical Timescales _____	56
Table 5.	Physical Properties of the Outflows _____	56
Table 6.	Physical Parameters of Other Outflows _____	59

LIST OF FIGURES

Figure 1.	An Accelerated Outflow Model _____	8
Figure 2.	A Decelerated Outflow Model _____	9
Figure 3.	Schematic Model for the Structure of a Molecular Flow _____	12
Figure 4.	$^{12}\text{CO } J = 2 \rightarrow 1$ Spectral Line Map for GL 490 (20" spacing) _____	20
Figure 5.	$^{12}\text{CO } J = 2 \rightarrow 1$ Spectral Line Map for GL 490 (10" spacing) _____	21
Figure 6.	$^{12}\text{CO } J = 2 \rightarrow 1$ Spectral Line Map for NGC 7538 IRS 9 (20" spacing) _____	22
Figure 7.	$^{12}\text{CO } J = 2 \rightarrow 1$ Spectral Line Map for NGC 7538 IRS 9 (10" spacing) _____	23
Figure 8.	^{13}CO Spectrum and Selected ^{12}CO Spectra for GL 490 _____	34
Figure 9.	Channel Maps for GL 490 _____	38
Figure 10.	Integrated Intensity in $\text{CO } J = 2 \rightarrow 1$ Emission for GL 490 _____	40
Figure 11.	Emission Centroid Positions for GL 490 _____	41
Figure 12.	Position-Velocity Map of CO emission for GL 490 _____	43
Figure 13.	Velocity Structure in Blue Wing of GL 490 _____	44
Figure 14.	^{13}CO Spectra and Corresponding ^{12}CO Spectra for NGC 7538 IRS 9 _____	47
Figure 15.	Channel Maps for NGC 7538 IRS 9 _____	50
Figure 16.	Integrated Intensity in $\text{CO } J = 2 \rightarrow 1$ Emission for NGC 7538 IRS 9 _____	52
Figure 17.	Emission Centroid Positions for NGC 7538 IRS 9 _____	53
Figure 18.	Position-Velocity Map of CO emission for NGC 7538 IRS 9 _____	54
Figure 19.	Mechanical Luminosity vs. Total Radiant Luminosity _____	60
Figure 20.	Momentum Flux vs. Total Radiant Luminosity _____	61

I. INTRODUCTION

Understanding the processes involved in star formation has become a major area of astronomical research, both theoretical and observational. Since star formation occurs in the dense cores of dark molecular clouds, the visual extinction is much too great to allow optical observations of these early stages of evolution. We must turn to regions of the spectrum where these clouds are transparent. Most advances in this field have been through observations at infrared and microwave wavelengths, where studies have revealed the presence of outflowing molecular gas with supersonic velocities of up to $160 \text{ km}\cdot\text{s}^{-1}$ (eg. Mitchell *et al.*, 1989; Koo, 1989; Lizano *et al.*, 1988). Observations have indicated the presence of circumstellar disks surrounding many sources of outflow (eg. Kawabe *et al.*, 1984, Campbell *et al.*, 1986, and Mundy & Adelman, 1988). The presence of circumstellar disks may also lead to a possible solution to the problem of how these outflows are being collimated. By studying the spectral line profiles of such molecules as NH_3 , CS , and CO we can determine the physical properties of such phenomena as mass outflows, high velocity water maser sources, and FU Ori objects.

Giant Molecular Clouds (GMCs) are the most active regions of star formation. It is within these GMCs that we can witness the early stages of stellar evolution. These structures are among the largest in the Galaxy, containing between 10^5 and $10^6 M_{\odot}$ of material and may be as large as 100 pc in their longest dimension. Solomon *et al.* (1985) suggest that there are two kinds of molecular clouds, cold ($T_{\text{gas}} \leq 10\text{K}$) and warm ($T_{\text{gas}} > 10\text{K}$). Stars located in cold clouds are usually found to be late B type or later and are present throughout the galactic disk while the stars located in warm clouds are often early B and O type stars and are concentrated along the spiral arms.

The distribution of material in GMCs tends to be clumpy and so collapse is not uniform over the entire cloud. The localized condensations are 2-5 pc in size and contain on the order of $10^3 - 10^4 M_{\odot}$. The cores of these clumps are much denser than the surrounding medium and may contain protostars which can be mapped in HC_3N , NH_3 , CS , and in CO (if the core gas temperature is warmer than the surrounding material). Millimeter-wave molecular line observations of CO are used to determine the dynamical and physical conditions of the cold gas surrounding these young stellar objects (YSOs).

a) **Star Forming Clouds**

One may calculate the critical mass of a molecular cloud for which the cloud is gravitationally stable. If the critical mass is exceeded, the cloud will collapse (assuming that only gravitational forces are present). The critical mass is called the Jeans mass and is written as

$$M_J \geq \left[\frac{\pi k T}{\mu G} \right]^{\frac{3}{2}} \rho^{-\frac{1}{2}},$$

where T is the cloud temperature and ρ is the cloud density (Spitzer, 1978). Most cloud cores have masses greater than the Jeans limit. If gravitational forces were the only forces acting on these cloud cores, collapse would be rapid and we would expect to see a high rate of star formation in these regions. Bally & Lada (1983) calculate a star formation rate of $\sim 10^3 M_{\odot}/\text{yr}$ in the Galaxy, assuming gravitational contraction with an average free-fall time of 10^6 years. Smith, Biermann, and Mezger (1978), however, determined the star formation rate for the Galaxy to be 1-10 M_{\odot}/yr , which is much lower than the expected rate obtained by Bally & Lada (1983). Clearly some other processes must support these clouds against gravitational contraction. Some of these processes may be turbulence, rotation, and magnetic fields (Shu *et al.*, 1987). By themselves they cannot hinder

collapse for very long but together they may stabilize the cloud for long times (the reasons for this are discussed below). However, instabilities in the system gradually grow and eventually collapse will begin.

If a molecular cloud is rotating, the rotation counteracts the gravitational field. If rotation is rapid enough collapse may be halted. However, observations of rotational velocities in these star forming cores show that they are too small to account for support against collapse (Arquilla & Goldsmith, 1986). The effects of a magnetic field are much stronger than those of rotation. The magnetic energy stored in a large cloud (~100 pc) can readily be comparable to the system's gravitational potential (Bowers & Deeming, 1984). The magnetic field resists compression of material perpendicular to the field lines but not parallel to the field, causing the cloud to flatten in a direction transverse to the magnetic field.

b) Evidence for Molecular Outflows

Present theories suggest that most or even all YSOs of low to intermediate mass may go through a period of energetic mass loss. Jaffe *et al.* (1981) find that approximately 70% of all luminous H₂O maser sources have associated high-velocity components, implying that high mass stars also go through a phase of energetic mass loss in the early stages of evolution. Mass loss may take the form of molecular outflows, strong stellar winds, or jets before the YSO evolves onto the main sequence. Evidence for mass loss includes broad millimeter-wave molecular emission lines, rapidly moving Herbig-Haro objects (HH objects), vibrationally excited H₂ emission regions which appear to be shock-excited, high velocity maser sources, and optically visible jets which appear to emanate from the region immediately surrounding the YSO.

We see evidence of mass loss in solar mass emission-line variable stars called T Tauri stars. T Tauri stars lie above the zero-age-main-sequence (ZAMS) and are believed to be still contracting toward the main sequence. Roughly 60% of all T Tauri stars exhibit a double-peaked structure in their emission-line profiles due to absorption on the blue side of the emission line (Lada, 1985). DeCampi (1981) interprets the presence of blue-shifted absorption features in the spectra of T Tauri stars as evidence of steady mass outflow from these objects.

High resolution infrared spectroscopy has revealed compact regions of hydrogen recombination emission surrounding many YSOs. Recombination lines exhibit profiles with full widths in excess of $100 \text{ km}\cdot\text{s}^{-1}$, much greater than expected from thermal motions ($\sim 30 \text{ km}\cdot\text{s}^{-1}$; Persson *et al.*, 1984). Lada (1985) suggests that these large velocity widths of the emission lines arise in circumstellar winds. Another example of mass loss is the FU Ori outburst phenomenon in which multiple absorption line components with blueshifts up to $180 \text{ km}\cdot\text{s}^{-1}$ relative to the ambient interstellar material are seen. Such a large shift is not typical of a continuous stellar wind and suggests intermittent mass ejection (Lada, 1985).

Excess high-velocity CO emission may be explained, in principle, by collapse, expansion, rotation, or turbulence. Through observations, however, we note that several characteristics of these sources imply that the broad lines result from an expansion (or outflow) of molecular gas. Bipolar structure, large spatial extents, and high velocities are the basic physical characteristics of these flows. We may rule out turbulence as an explanation since it does not account for bipolar structure. Collimated collapse may be ruled out on energetic grounds because observed velocities are much greater than the few $\text{km}\cdot\text{s}^{-1}$ possible during free-fall. Rotation and collimated expansion models could explain the spatial structure of the sources. However, observations of rotational velocities indicate

that rotation alone cannot account for the observed high velocities of the gas, nor is it able to account for the large spatial extent of the emission.

We may use the virial theorem to determine the interior mass required to confine a rotational structure. The virial theorem gives us $M \geq v^2 r / 2G$, where v is the observed velocity and r is the spatial extent. If a source has a spatial extent greater than a few tenths of a parsec and a velocity greater than $10 \text{ km}\cdot\text{s}^{-1}$, an interior mass greater than $10^4 M_{\odot}$ is required to confine the rotational structure. Observations indicate, however, that the total mass of the ambient gas within molecular cloud cores is often much less (by more than a factor of 10^4 ; Lada & Harvey, 1981). Although the mass is determined using the column density of gas in line cores, there is no evidence for enough extra mass of a non-molecular nature to confine the flow, implying that a model based on gravitationally bound motions (such as a rotational model) cannot adequately explain the kinematics of most flow sources (Lada, 1985). By the process of elimination we conclude that high-velocity molecular flows are anisotropic mass outflows from YSOs.

Some evidence that these high-velocity molecular flows are indeed anisotropic mass outflows are their association with HH objects and water maser sources. As an example, observations of proper motions of water maser sources located within the Orion molecular flow indicate a directed expansion of maser sources away from an IR source buried deep in the cloud (Genzel *et al.*, 1981). Proper motion measurements of the HH objects located in blueshifted lobes of highly collimated flows provide another example of an anisotropic mass outflow. Herbig & Jones (1981, 1983) have detected very large proper motions for many objects and infer very high tangential velocities ($200\text{-}350 \text{ km}\cdot\text{s}^{-1}$). High tangential velocities are indicative of a high-velocity outflow phenomenon, given that some HH objects also exhibit high radial velocities of a similar magnitude and that they are predominantly blueshifted with respect to the dark clouds within which they are imbedded

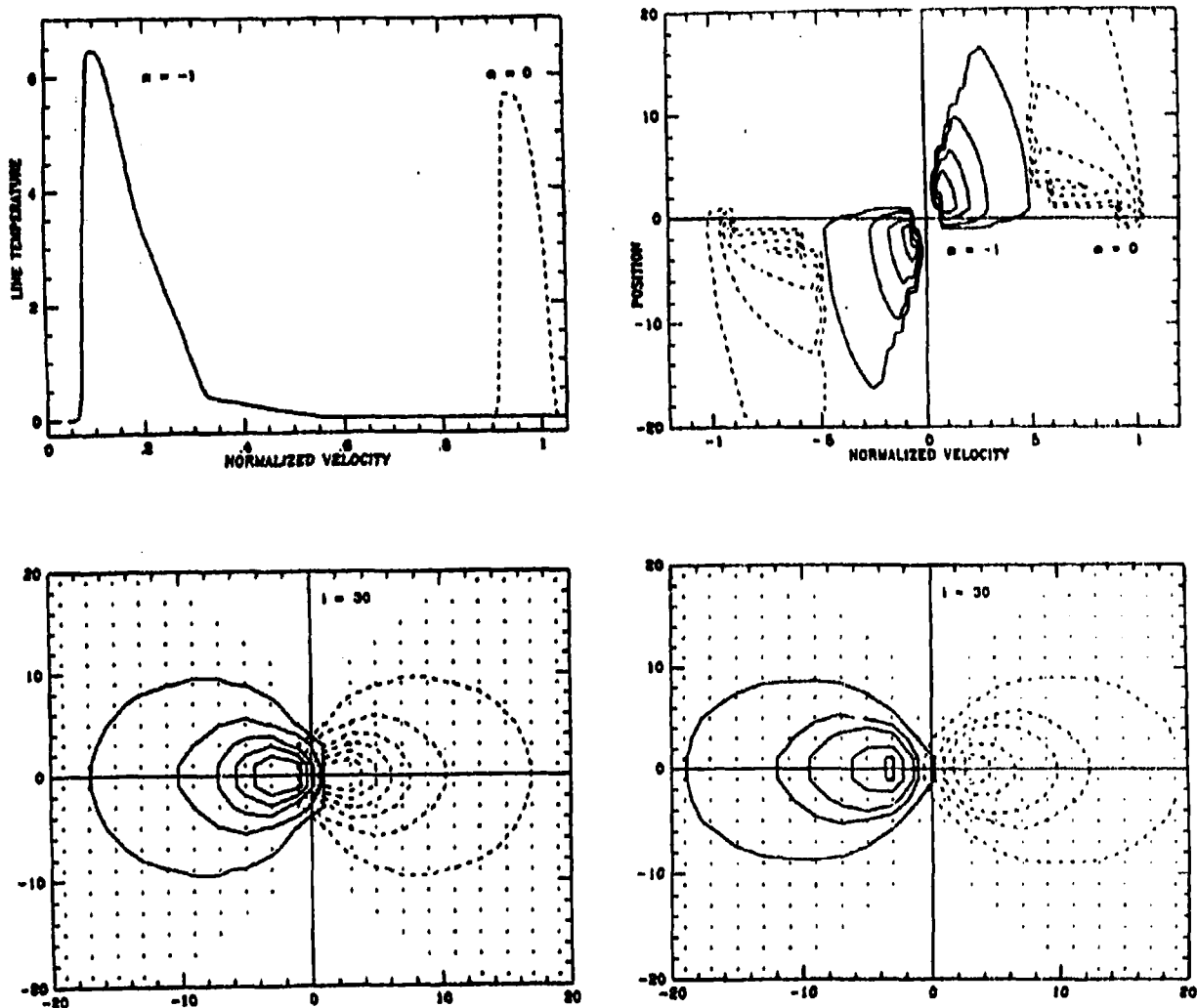
(Strom *et al.*, 1974). Since HH objects and water maser sources are high-velocity flows it could well be likely that their kinematics are also typical for all high-velocity flows.

Another strong piece of evidence that the broad molecular lines are produced by outflow is the detection of vibrationally excited molecular hydrogen quadrupole emission lines at 2- μm in many molecular flows (eg. Shull & Beckwith, 1982). The high gas temperatures implied by the extended H₂ emission lines observed in Orion suggests that the emitting gas is collisionally excited behind a shock front which may be due to the interaction between the high-velocity CO flow and the ambient cloud material (eg. Shull & Beckwith, 1982). Erickson *et al.* (1982) find that the brightest H₂ emission is found at the periphery of the CO flow, which also suggests outflow rather than inflow. Scoville *et al.* (1986) state that observations of H₂ emission at the outer extent of the molecular flow imply a shock front where outflowing gas interacts with the quiescent cloud which, in turn, implies that the gas is driven by the YSO. By studying how high-velocity flows interact with the external quiescent molecular cloud we may obtain clues to the processes involved in star formation. These interactions may even induce more star formation (Kameya *et al.*, 1989).

Determining the actual outflow mechanism and understanding the relationship between the inner winds and the spatially extended flows poses a problem for present theories (Mitchell *et al.*, 1991). The energies inferred for typical outflows are in the range of 10^{43} - 10^{47} ergs. Thus, these outflows may be a significant energy source for GMCs and may also be a major factor in the stability of such a cloud (Margulis & Lada, 1985). Stellar winds alone cannot account for the large energies observed, implying that other mechanisms may be involved. The FU Ori phenomenon, which Herbig (1977) concluded to be a stage which occurs many times in every T Tauri type star, may provide an important clue. FU Ori eruptions are thought to be driven by disk accretion and it follows

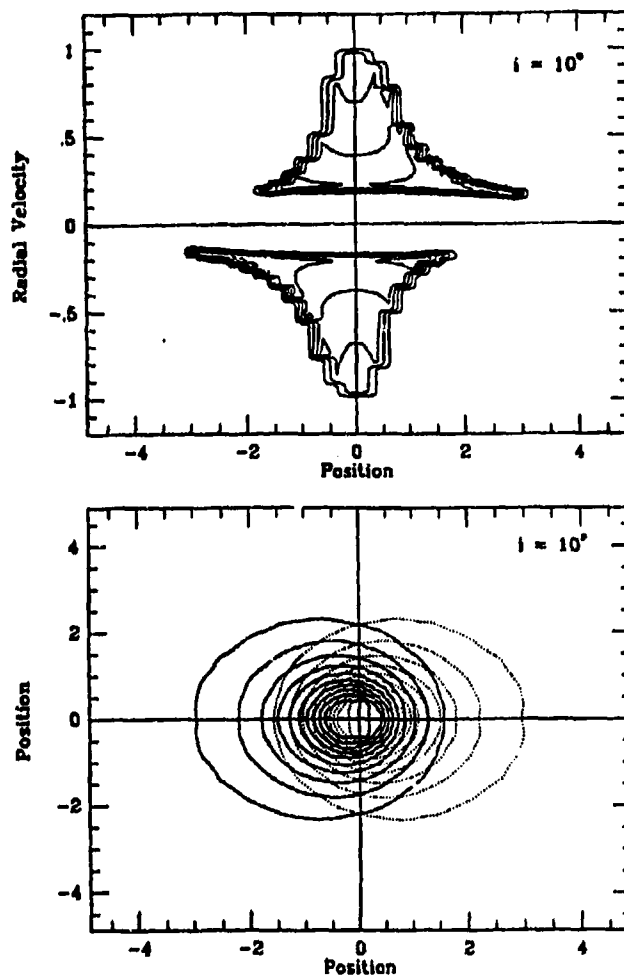
that these eruptions may occur more frequently in young stars which are deeply embedded in molecular clouds and accreting rapidly. Reipurth (1990) suggests that many embedded infrared sources are characterized by FU Ori eruptions.

Outflows often show a bipolar nature with a high degree of collimation close to the driving object and a decreasing degree of collimation farther away (Phillips *et al.*, 1988). By studying the characteristics of the velocity field as it varies across the mapped region we may gain some important insight regarding the flow structure and dynamical evolution. By constructing position-velocity CO maps (eg. Figures 12 and 18) we can see that the velocity fields of the ambient cloud and that of the molecular flow are quite distinct from each other. Secondly, the velocity gradient between the ambient cloud and the molecular flow is very steep implying rapid acceleration or deceleration of the swept-up ambient material at the periphery of the flow. Two papers by Cabrit & Bertout (1986 & 1990) discuss models for accelerated and decelerated CO outflows. Figures 1 and 2 show models for accelerated and decelerated outflows respectively (from Cabrit & Bertout (1986 & 1990) for the CO $J = 1 \rightarrow 0$ transition). These models use a cone opening angle $\theta_{\max} = 30^\circ$ and an inclination angle $\theta = 30^\circ$ for the accelerated case and $\theta = 10^\circ$ for the decelerated case. We may compare our position-velocity maps with these models to determine the nature of our sources. Finally, we can infer the presence of a thin swept-up shell which surrounds an evacuated wind cavity by noting the near spatial coincidence of the high and low velocity outflow gas in some sources (Snell *et al.*, 1984). Strong evidence of this hypothesis lies in a high resolution study of L1551 by Kaifu *et al.* (1985). Their observations show that the high-velocity gas is located at the inner edge of a shell surrounding an evacuated cavity, while the lower-velocity gas is found near the outer edge of the shell.



—Results for a cone opening angle of 30° and an inclination angle $i = 30^\circ$ corresponding to case 1 (see text for details and for the values of other parameters). (upper left) Profile of the $^{12}\text{CO } J = 1 \rightarrow 0$ line for the sight line crossing the molecular flow closest to the stellar core. The solid line is for case $\alpha = -1$, the dashed line for $\alpha = 0$. (upper right) Velocity vs. position map, showing contours of constant line temperature for $\alpha = -1$ (solid lines) and $\alpha = 0$ (dashed lines). Lowest contour level, 0.1 K; second one, 1 K; step between other contours, 2 K. Off in units of $r_{\text{out}}/4$. (lower left) Map of blue (solid lines) and red (dashed lines) integrated intensity for $\alpha = -1$. Emergent intensities computed at positions indicated by crosses. Contour levels K km s^{-1} and distance scale as in upper right panel. (lower right) Same as lower left for $\alpha = 0$. Lowest contour level, 1 K km s^{-1} ; second one, 3 K km s^{-1} ; step between other contours, 1 km s^{-1} .

Figure 1. (Cabrit & Bertout, 1986) Accelerated outflow model results for two types of line profile: $\alpha = 0$ for a narrow line wings and $\alpha = -1$ for broad line wings. The $\alpha = -1$ case is relevant to this thesis. Position-velocity diagrams are for CO emission along the major axis of the outflow. Velocity increases with distance from the source position. The quantity r_{min} is the radius of the narrowest part of the outflow cone. The line core was omitted for clarity.



—Results for a cone opening angle of 30° and an inclination angle ($i = 10^\circ$, illustrating case 1 (see text for values of other parameters). *Upper panel:* Spatial-velocity diagram showing contours of constant CO $J = 1 \rightarrow 0$ line temperature along the flow axis. Radial velocities are in units of v_{max} and position offsets in units of r_{max} . Lowest contour level, 0.1 K; second one, 1 K; step between other contours, 1 K. *Lower panel:* Contour map of integrated intensity in the blueshifted (solid lines) and redshifted (dashed lines) CO $J = 1 \rightarrow 0$ emission. Position offsets are in units of r_{max} . Lowest contour level $0.1 \text{ K} \times v_{\text{max}}$, step between contours, $0.2 \text{ K} \times r_{\text{max}}$.

Figure 2. (Cabrit & Bertout, 1990) Decelerated outflow model results. The velocity and position axes in the position-velocity diagram have been switched with respect to Figure 1. Radial velocities are normalized to v_{max} . Position-velocity diagrams are for CO emission along the major axis of the outflow. Velocity decreases with distance from the source position. The line core was omitted for clarity.

A study of individual CO profiles for outflow sources show most emission to be at the lowest flow velocities. Lada (1985) indicates that this may be the result of a low beam-filling factor of the higher velocity gas compared to the higher beam-filling factor of the lower velocity gas (the beam-filling factor is the fraction of the total area covered by the antenna beam which contains the desired source). The low beam filling factor of the high-velocity gas may be misleading since the smaller, less easily observed clumps (ie. low beam-filling factor) in the flow may be moving at higher velocities than the larger clumps (Goldsmith *et al.*, 1984). Another explanation might be that clumps of similar sizes are accelerated to the outer edge of the wind cavity. When these accelerated clumps interact with the ambient cloud they collide with, and sweep up the ambient material, causing the clumps to decelerate. Observations of L1551 made by Kaifu *et al.* (1985) indicate such an interaction and subsequent deceleration. A schematic model showing the structure of a molecular outflow is shown in Figure 3 (Lada, 1985). In this model the cold molecular gas is accelerated inside the wind cavity until, at some point, it is carried to the inner edge of the swept-up shell. There it interacts with the material in the shell, causing the clump to decelerate as it sweeps up material, thus resulting in the clump having a larger beam-filling factor than the clumps on the inner edge of the shell. The two sources studied in this paper, GL 490 and NGC 7538 IRS 9, show evidence for the mass outflow process.

A number of mechanisms have been proposed which produce high velocity molecular gas outflows. A stellar wind model and a disk wind model are discussed briefly below:

(1) After a protostar has formed inside the molecular cloud core, strong stellar winds are generated by the protostar. The stellar winds are forced out of the regions of the cloud core where the density is the lowest, namely the rotational poles (Shu *et al.*, 1987). A problem with a stellar wind model arises, however, when one compares the observed momentum flux, $\dot{M}V$, with the force exerted on the gas if every photon emitted by the central source is absorbed, L^*/c . Observations show that the momentum flux is larger

than L^*/c by two to three orders of magnitude implying that the observed ionized winds cannot drive the extended flows (eg. Lada, 1985).

(2) A model using winds originating from a magnetized accretion disk as a driving mechanism was developed by Pudritz & Norman (1983, 1986) and Pudritz (1985). The model requires that magnetic field lines be aligned with the rotation axis of a large and massive disk (radius ≈ 5000 AU, mass $\approx 100 M_{\odot}$). Gas is driven outward if the magnetic field lines corotate with the disk. Winds originating from the inner disk are expected to be ionized, while the outer disk drives a molecular wind (assuming the fractional ionization is high enough to allow strong ion-neutral coupling, Mitchell *et al.* 1991). The outer disk drives a faster mass accretion than the inner disk, resulting in a mass pileup at the boundary between the inner disk and the outer disk. Mass accumulation can lead to various instabilities which may cause an outburst, the result of which is a mass outflow. Pudritz & Norman (1986) show that this model may explain such phenomena as the observed momentum flux and the observed high degree of collimation. The model may also account for the multiple velocity features observed in many objects.

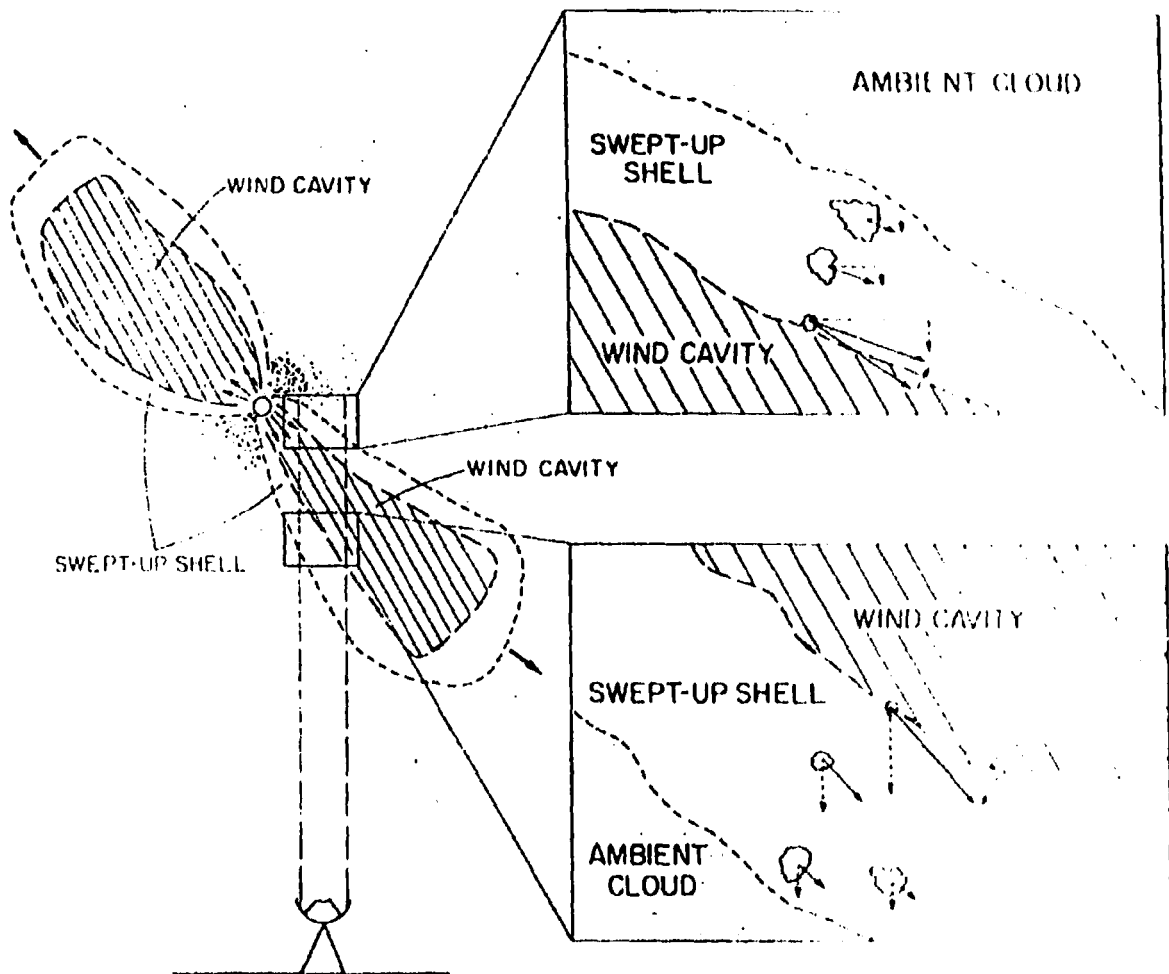


Figure 3. (from Lada 1985) A schematic model for the structure of a molecular flow, derived from observations of a few well-studied examples. In this model, cold molecular gas is accelerated and swept up into a relatively thin shell at the edge of a stellar cavity. At the interface between the cavity and the shell, cloud clumps are accelerated to high velocities in a direction mostly parallel to the cavity-shell interface as shown. The accelerated clumps will inevitably have a component of velocity that drives them into the shell, and as they traverse the shell, they sweep up ambient gas and decelerate. Consequently, material at the outer edge of the shell will be moving with lower velocity and have a larger beam filling factor than material at the shell's inner edge. Line profile shapes of outflow sources show that most of the material in a flow is observed at relatively low projected velocities. An observation taken along the line of sight shown will detect outflow material with blueshifted radial velocities only. In the diagram the line-of-sight component of a clump's velocity vector is drawn as a dashed arrow. The detailed shape of an observed line profile will depend primarily on the orientation or inclination of the flow with respect to the observer.

c) GL 490 Background

GL 490 (at $\alpha(1950) = 3^{\text{h}}23^{\text{m}}38^{\text{s}}.8$ and $\delta(1950) = 58^{\circ}36'39''$ and galactic coordinates, $l = 142^{\circ}$ and $b = +2^{\circ}$) is a strong IR source believed to be an obscured protostellar object. Snell *et al.* (1984) derive a distance of 1.0 ± 0.5 kpc to GL 490, assuming a flat galactic rotation curve at $R > R_0$ and a $6 \text{ km}\cdot\text{s}^{-1}$ (rms) random motion for molecular clouds with diameters greater than 20 pc. Morris *et al.* (1974) observed HCN and CS at millimeter wavelengths centered on the IR source position and concluded that GL 490 was embedded in a dense molecular cloud. Minchin *et al.* (1991) indicate that a surrounding, near-infrared reflection nebula is being illuminated by GL 490. Their findings are based on the appearance of a centro-symmetric pattern in a high-resolution polarization vector map centered on the IR source. A study in the near IR by Merrill *et al.* (1976) revealed "ice" and silicate absorption features similar to those of the BN object in Orion (*ie.* a very young star surrounded by a thick dust shell). From far IR observations, the bolometric luminosity is $L \sim 1.4 \times 10^3 L_{\odot}$ (using an assumed distance of 1 kpc), which is that of a ZAMS B3 star (Harvey *et al.*, 1979).

Thompson & Tokunaga (1979) determine that the Lyman continuum flux from GL 490 (inferred from the $\text{Br}\gamma$ line strength) is ~ 100 times the Lyman continuum flux expected of a main sequence star whose luminosity is similar to the total infrared luminosity of GL 490. The expected Lyman continuum flux assumed that most of the neutral hydrogen in the ionized region is in the $n=1$ energy level. The problem of this apparent excess ultraviolet flux was addressed by Simon *et al.* (1983) who state that, at the temperatures typical for early B type ZAMS stars, only a small fraction of the photon flux is in the Lyman continuum. The bulk of the photon flux will be in the Balmer continuum (*ie.* photoionization of H from the $n = 2$ energy level rather than $n = 1$). If enough hydrogen is in the $n = 2$ energy level an excess amount of ionization and recombination-line fluxes are

produced compared to those expected in classical photoionization HII regions. Therefore, GL 490 may not be overluminous. Such a theory requires that the material surrounding GL 490 be optically thick.

Using CS emission observations, Kawabe *et al.* (1984) have detected the presence of a large disk with dimensions 0.3×0.13 pc surrounding GL 490. The disk appears to be elongated in a direction perpendicular to the CO outflow. Evidence for a small-scale disk surrounding GL 490 is demonstrated by Mundy and Adelman (1988) whose observations using the 2.7 mm continuum have resolved a structure 2600×1500 AU around the source, which they think may be a circumstellar disk. Optical CCD images of a possible disk surrounding GL 490 were obtained by Campbell *et al.* (1986). Their observations have indicated the presence of a large-scale diffuse cone of emission which extends out to 0.8 pc from the infrared source and corresponds fairly well to the blueshifted CO emission. One of their images of the core region has resolved a structure 700-1000 AU in diameter and appears to be elongated perpendicular to the CO outflow.

Using near-infrared imaging polarimetry, Hodapp (1984) found that the position angle of polarization remained fairly constant with wavelength in a direction perpendicular to the CO outflow. He believes this to be caused by a scattering of radiation due to grains in a disk also oriented orthogonal to the molecular outflow. He further states that this indicates that the CO outflow is collimated by interacting with the disk or the magnetic field. In a later paper, Hodapp (1990) measured the position angle of polarization for background stars close to the star forming region to determine the local projected magnetic field direction. His results for GL 490 were different from the other two outflow sources he studied in that the outflow direction is almost perpendicular to the local magnetic field.

Lada & Harvey (1981) were the first to detect broad ^{12}CO emission wings around the GL 490 IR source. Using a 66" half-power beamwidth (HPBW), Lada & Harvey (1981) observed that the red and blue emission peaks were separated by 67" and appeared to be centered on the IR source. Using a smaller beam (48" HPBW) and 30" spacing Snell *et al.* (1984) found that the center of the line connecting the blue and red emission peaks was located 34" southwest of the GL 490 IR source. Margulis & Lada (1985) obtained similar results using a 66" HPBW. These results cast doubt on GL 490 being the source of the outflow. Using interferometer measurements of ^{13}CO emission Mundy & Adelman (1988) found a red-shifted clump ($13" \times 7"$ in size) lying $\sim 6"$ southeast of GL 490. Since the results obtained by Snell *et al.* (1984) and Margulis & Lada (1985) show the center of the ^{12}CO red-shifted wing to lie north of GL 490 it is probable that the ^{13}CO clump is not related to the large outflow.

d) NGC 7538 IRS 9 Background

NGC 7538 is a complex HII region found in the Perseus spiral arm and can be seen on the Palomar Sky Survey. Werner *et al.* (1979) discovered the high-density core region of the NGC 7538 molecular cloud to be an area of active star-formation containing five bright IR sources (IRS 1, 2, 3, 9, and 11) all within a $3'5 \times 3'5$ area. Three regions show indications of high-velocity flows close to the IR sources, one of which is IRS 9. NGC 7538 IRS 9 is located at $\alpha(1950) = 23^{\text{h}}11^{\text{m}}52^{\text{s}}.8$ and $\delta(1950) = 61^{\circ}10'59''$ (galactic coordinates, $l = 112^{\circ}$ and $b = +1^{\circ}$) with an assumed distance of 2.7 kpc (Kameya *et al.*, 1989). IRS 9 has a measured luminosity of approximately $4 \times 10^4 L_{\odot}$ at the assumed distance of 2.7 kpc.

Using observations at $2 \mu\text{m}$, Werner *et al.* (1979) discovered a large region of extended near-infrared emission to the south of IRS 9 which is most likely a reflection

nebula. They also note the presence of grains hot enough to emit at 50 μm and suggest that, along with the reflection nebula located nearby, this indicates that IRS 9 is located in a fairly dusty region. Kameya *et al.* (1989) find that the apparent structure of the blueshifted outflow component appears somewhat shell-like and seems to delineate the nearby reflection nebula. Polarization studies of the reflection nebula at 3 μm by Tokunaga *et al.* (1981), show that the direction and degree of polarization are consistent with a normal reflection nebula. Campbell and Persson (1988) and Eiroa, Lenzen, and Gomez (1988) observe the reflection nebula on optical CCD images thus concluding that the visual extinction is not so large as to obscure the optical emission entirely in the regions not immediately surrounding the IR source.

Kameya *et al.* (1989) note that the brightness of the reflection nebula decreases sharply toward IRS 9. Since it appears that the reflection nebula may be associated with the blueshifted gas this implies that only the near side of the outflow in the reflection nebula is visible. If this is the case, then the part of the redshifted flow closest to IRS 9 may not be visible due to extinction caused by a disk around the IR source. To substantiate the possible existence of a disk surrounding IRS 9, Werner *et al.* (1979) locate a region of high visual extinction to the north and east of IRS 9 using infrared observations. Eiroa, Lenzen, and Gomez (1988) find this visual extinction to be larger than 25.4 magnitudes. Campbell and Persson (1988) and Eiroa, Lenzen, and Gomez (1988) also observe a dark lane between the two diffuse nebula on the CCD images oriented almost perpendicular (NE-SW) to the molecular outflow. They believe that this suggests the presence of a circumstellar disk.

Kameya *et al.* (1989), in a study of the CO $J = 1 \rightarrow 0$ transition, determined that high-velocity gas was present but could not conclusively prove that bipolarity of the outflow existed. Their data was not conclusive due to the weakness of the line wings in the $J =$

1→0 transition. A study of the CO J = 2→1 transition should clarify the presence of bipolarity since the CO J = 2→1 line wings are stronger and broader than the CO J = 1→0 line wings. Other evidence for the presence of high-velocity outflows from IRS 9 exists in the observations of $v = 1 \rightarrow 0$ S(1) line emission from H₂ at the position of the reflection nebula (Fischer *et al.*, 1980). The emission arises in hot gas (~2000 K). The high gas temperatures suggest that the gas emitting the H₂ lines is collisionally excited behind a shock front. The shock front probably arises from an interaction between the CO outflow and the ambient cloud material.

Werner *et al.* (1979) note that the result of a low upper limit in radio emission as well as the shape of the 1-20 μm energy distribution and the location of IRS 9 in a star forming cloud strongly suggests the presence of a massive protostar. The fact that IRS 9 is well-separated from the other IR sources in the NGC 7538 core makes it a useful target for the study of massive star formation.

II. OBSERVATIONS AND DATA ANALYSIS

a) Equipment Used

This thesis is based on ^{12}CO $J = 2 \rightarrow 1$ and ^{13}CO $J = 2 \rightarrow 1$ observations carried out in August 1989 by G.F. Mitchell and T.I. Hasegawa using the 15-m James Clerk Maxwell telescope on Mauna Kea, Hawaii. One of the "common-user" receivers was used, receiver A at 230 GHz. Receiver A uses two mixer sets to achieve its frequency range of 220 - 280 GHz. The acousto-optical spectrometer (AOSC) with a bandwidth of 500 MHz, provided a total bandwidth of $650 \text{ km}\cdot\text{s}^{-1}$ at 230 GHz. Operating at 230 GHz, the half power beamwidth (HPBW) was 21". The main beam efficiency was 0.71. There is an $\sim 10\%$ uncertainty in the beam efficiency. The observed intensity is obtained in the form of the antenna temperature, T_A^* . The accuracy of the conversion to antenna temperature is estimated to be better than 15%. Pointing was checked frequently each night and was found to be accurate to 3".

The ^{12}CO spectral data comprises a grid using 20" spacing (see Fig. 4 for GL 490 and Fig. 6 for NGC 7538 IRS 9) and a grid using 10" spacing (see Fig. 5 for GL 490 and Fig. 7 for NGC 7538 IRS 9) which is centered on the IR source. The HPBW (21") is defined such that the telescope receives approximately half of the total signal within this area. The data for the 10" spacing was integrated longer than the 20" data in order to obtain a higher signal-to-noise ratio so that the physical characteristics close to the source may be determined more accurately. Linear baselines were removed from the spectra to produce a common baseline at zero intensity.

For NGC 7538 the spectral data is in the form of a 49 point grid using 20" spacing and a 9 point grid using 10" spacing. Each position on the 20" grid was integrated for 32

seconds while each position on the 10" grid was integrated for 320 seconds. Only three positions were observed in ^{13}CO . These were at the offset positions of: (0, 0), (0, +20"), and (-20", -40"). For GL 490 the spectral data forms an 81 point grid using 20" spacing and a 9 point grid using 10" spacing. Each position on the 20" grid was integrated for 64 seconds while each position on the 10" grid was integrated for 320 seconds. ^{13}CO spectral data was obtained for the (0, 0) position only. Integration time for all ^{13}CO spectral data was 256 seconds. The channel size for the data in all ^{12}CO and ^{13}CO profiles was $\Delta\nu = .2484$ MHz. For the ^{12}CO data the observed frequency was 230.538 GHz which corresponds to a velocity resolution, $\Delta V_{\text{LSR}} = 0.323 \text{ km}\cdot\text{s}^{-1}$. For the ^{13}CO data the observed frequency was 220.3987 GHz which corresponds to a velocity resolution, $\Delta V_{\text{LSR}} = 0.339 \text{ km}\cdot\text{s}^{-1}$. Table 1 lists the observations for both objects.

TABLE 1
LIST OF OBSERVATIONS

Source	$^{12}\text{CO J} = 2 \rightarrow 1$	$^{13}\text{CO J} = 2 \rightarrow 1$
GL 490	9×9 map, 20" spacing 3×3 map, 10" spacing	(0,0) only
NGC 7538 IRS 9	7×7 map, 20" spacing 3×3 map, 10" spacing	(0,0), (0, N20), (E20,S40)

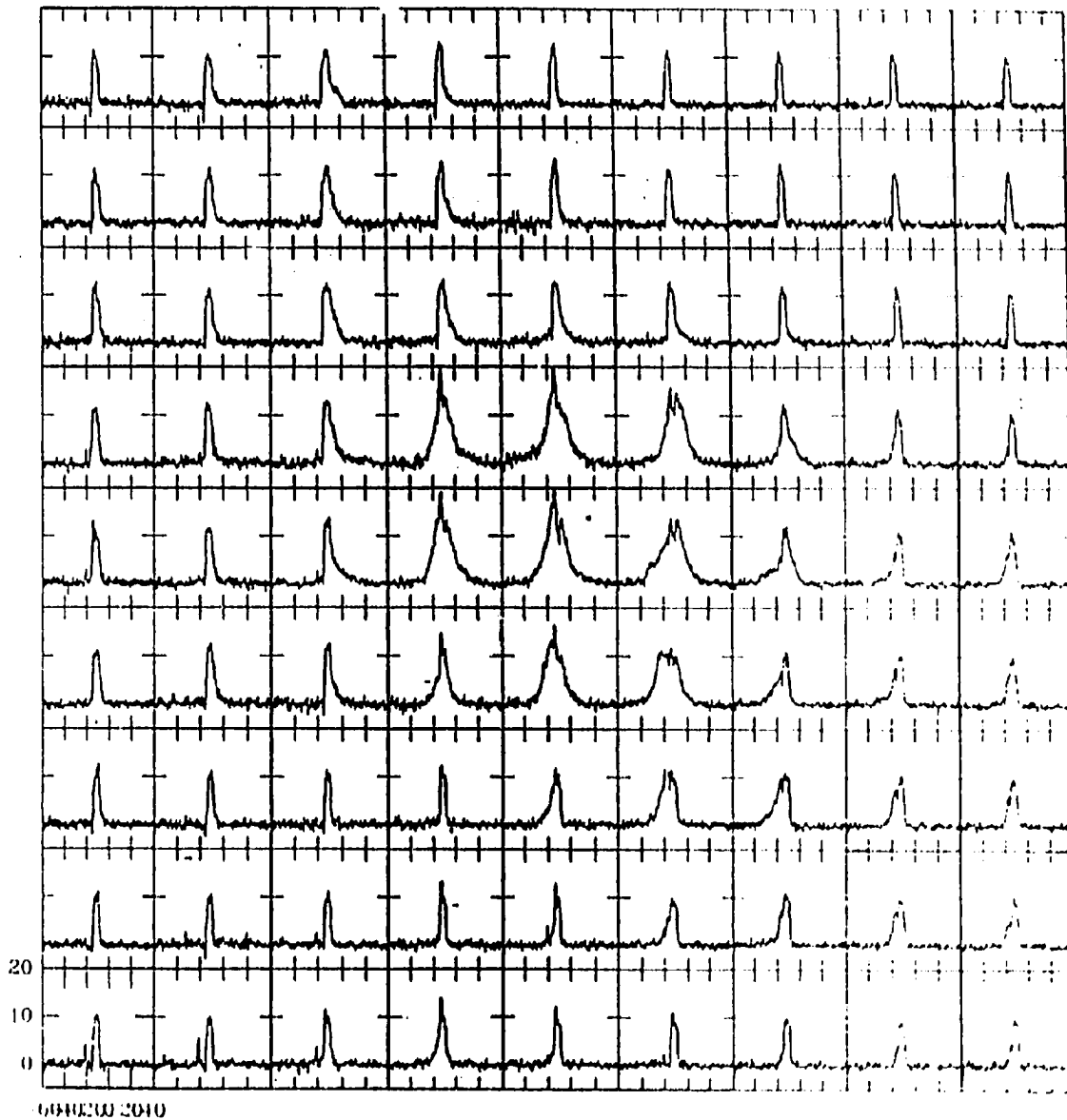


Figure 4. A $^{12}\text{CO } J = 2 \rightarrow 1$ spectral line map centered on GL 490 (R.A. = $3^{\text{h}}23^{\text{m}}39.0^{\text{s}}$, Dec. = $+58^{\circ}36'35''$). Each square represents the $^{12}\text{CO } J = 2 \rightarrow 1$ spectral line at that position (antenna temperature vs. V_{LSR}). In a given square each division on the x-axis is $20 \text{ km}\cdot\text{s}^{-1}$ while each division on the y-axis is 10 K. North is at the top and East is to the left. This map uses $20''$ grid spacing. Very broad line wings are observed for the inner 3×3 part of the map.

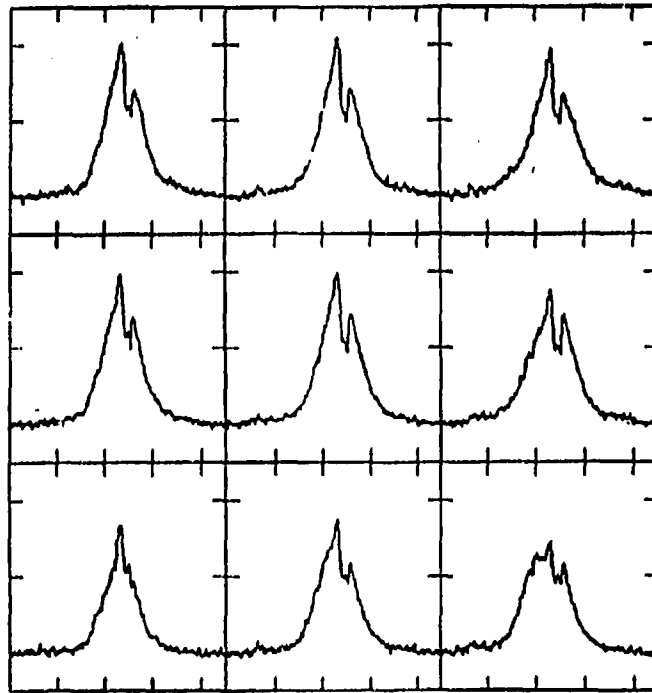


Figure 5. A 3×3 $^{12}\text{CO } J=2 \rightarrow 1$ spectral line map centered on GL 490. Each square represents the $^{12}\text{CO } J=2 \rightarrow 1$ spectral line at that position (antenna temperature vs. V_{LSR}). In a given square each division on the x-axis is $20 \text{ km} \cdot \text{s}^{-1}$ while each division on the y-axis is 10 K. North is at the top and East is to the left. $10''$ grid spacing was used. This map has a high S/N ratio and the line wings are very broad.

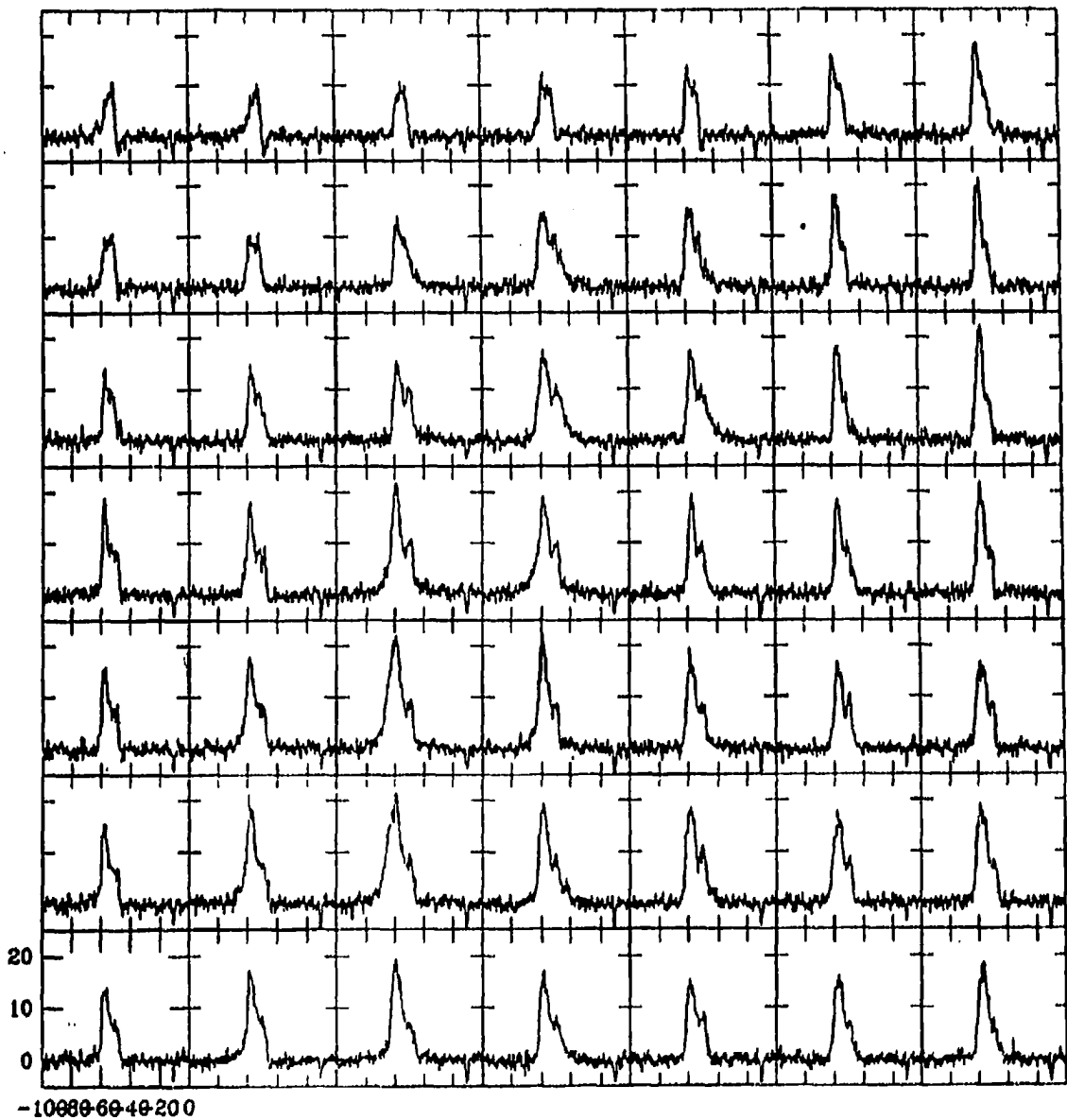


Figure 6. A $^{12}\text{CO } J = 2 \rightarrow 1$ spectral line map centered on NGC 7538 IRS 9 (R.A. = $23^{\text{h}}11^{\text{m}}52.8^{\text{s}}$, Dec. = $+61^{\circ}10'59''$). Each square represents the $^{12}\text{CO } J = 2 \rightarrow 1$ spectral line at that position (antenna temperature vs. V_{LSR}). In a given square each division on the x-axis is $20 \text{ km} \cdot \text{s}^{-1}$ while each division on the y-axis is 10 K. North is at the top and East is to the left. This map uses $20''$ grid spacing.

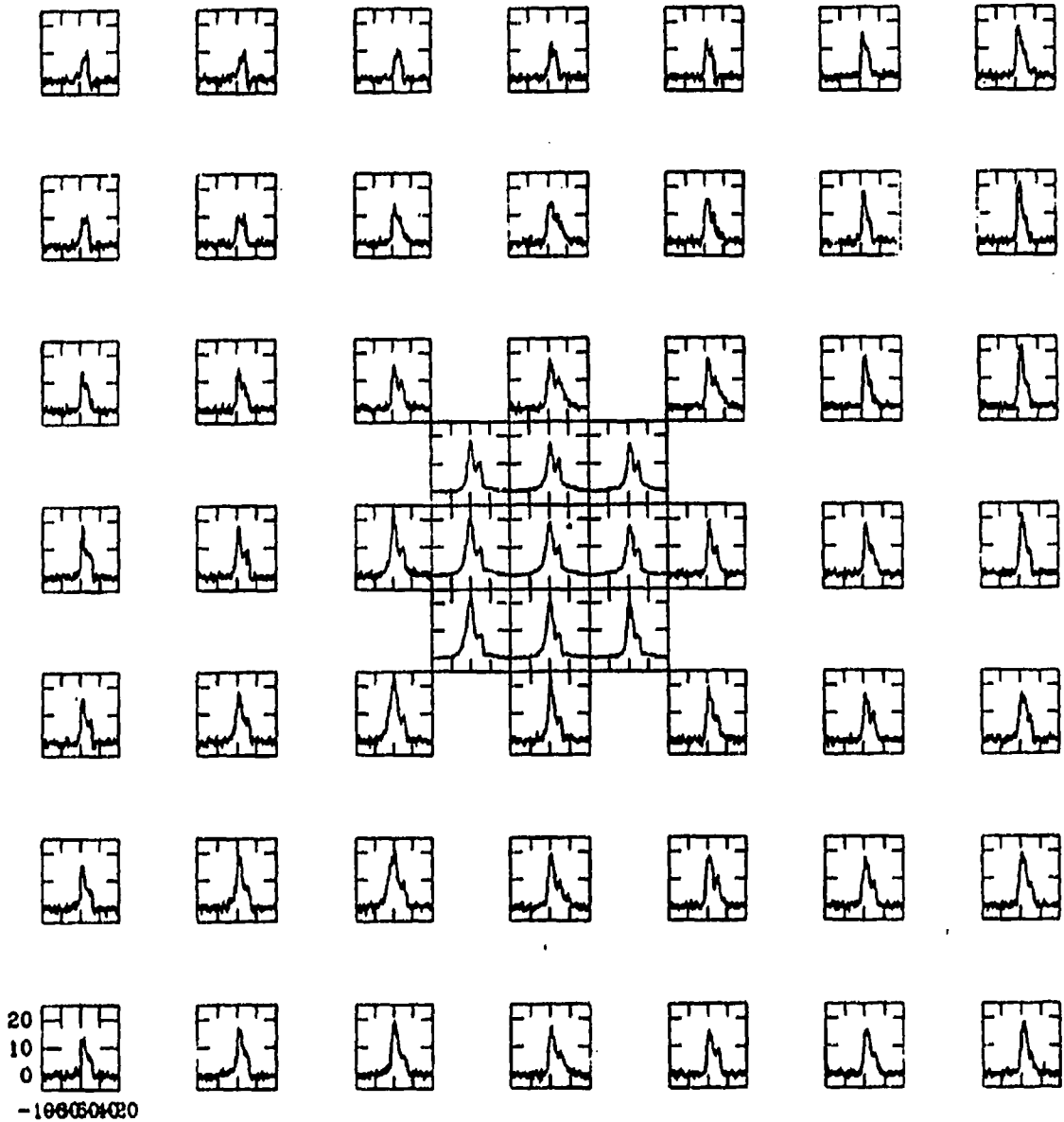


Figure 7. A 3×3 $^{12}\text{CO } J = 2 \rightarrow 1$ spectral line map centered on NGC 7538 IRS 9. Each square represents the $^{12}\text{CO } J = 2 \rightarrow 1$ spectral line at that position (antenna temperature vs. V_{LSR}). In a given square each division on the x-axis is $20 \text{ km}\cdot\text{s}^{-1}$ while each division on the y-axis is 10 K. North is at the top and East is to the left. $10''$ grid spacing was used. The spectra from the $20''$ map is also shown. The 3×3 map has a high S/N ratio and the spectra exhibit very broad line wings.

b) Reduction Programs

The $^{12}\text{CO } J = 2 \rightarrow 1$ and $^{13}\text{CO } J = 2 \rightarrow 1$ data were reduced using a reduction program called SPECX-V5.3 (Padman, 1988). This package allows the user to perform various forms of data manipulation. Baseline removal and the ability to produce contour plots and channel maps as well as being able to average several spectra together make SPECX a very useful tool for data manipulation. Linear baseline removal is useful since the data taken at the telescope is often offset from zero intensity and SPECX allows us to set the baseline to zero intensity. We use averaging in the cases where more than one spectrum was obtained for a given position. The spectra are averaged together to provide a single usable spectrum where the noise level is reduced by \sqrt{n} ($n \equiv$ number of spectra averaged). SPECX allows for the averaging of spectra with different integration times.

It was determined that the best approach to the data reduction was to take the raw spectral data from SPECX (which is in the form T_A^* vs. channel) and transfer it to another directory whereupon we used two FORTRAN programs, written specifically for this thesis, to calculate various quantities of which the end results were mass, momentum, and kinetic energy of the outflow for each offset position of the mapped region. The program PROFILE.FOR can be used to calculate line ratios if both ^{12}CO and ^{13}CO profiles are available, allowing us to calculate the ^{12}CO and ^{13}CO optical depth and excitation temperature, T_{ex} . We may also use this program to calculate CO column density for every channel. COLDEN.FOR takes the column densities and converts them into mass, momentum, and kinetic energy. A step-by-step explanation for the transferring of the SPECX data to another directory as well as for the use of the two FORTRAN reduction programs (PROFILE.FOR and COLDEN.FOR) may be found in Appendix A. Listings of PROFILE.FOR and COLDEN.FOR are found in Appendix B. In the next section we

discuss the theory involved in analyzing the T_A^* vs. channel data and converting it into mass, momentum, and kinetic energy of the high velocity gas.

c) Derivations of Important Physical Parameters

The first step in the analysis involves converting the raw data into a more usable form (i.e. changing T_A^* vs. channel into T_A^* vs. \mathcal{V}_{LSR} , where \mathcal{V}_{LSR} is the velocity of the gas with respect to the local standard of rest). Although SPECX converts channels into the corresponding \mathcal{V}_{LSR} we were not able to extract this information in a usable form. For this reason we need to calculate \mathcal{V}_{LSR} for each channel, which is accomplished by first calculating the velocity interval, $\Delta\mathcal{V}$. $\Delta\mathcal{V}$ is the velocity interval between any two adjacent channels. This involves the observed frequency interval, $\Delta\nu$, and the rest frequency, ν_o , through the relation

$$\Delta\mathcal{V} = \frac{c \cdot \Delta\nu}{\nu_o} . \quad (1)$$

Once we have calculated the velocity interval we then determine the zero channel, b_o , which corresponds to $\mathcal{V}_{LSR} = 0$. The zero channel is found by the equation,

$$b_o = b_c - \frac{(\nu_{obs} - \nu_o)}{\Delta\nu} , \quad (2)$$

where ν_{obs} is the observed frequency and b_c is the central channel. Once the zero channel and the velocity interval are known we can calculate \mathcal{V}_{LSR} for the center of each channel starting at the zero channel.

The next step involves converting the antenna temperature at each channel into the radiation temperature, T_R , using the relation $T_R = T_A^*/\eta f$, where η is the beam efficiency and f is the source filling factor. For our purposes we assume that the emitting high velocity gas fills the beam (*i.e.* $f = 1$) though Margulis & Lada (1985) find that the filling factors are much less than one for high velocity gas. This implies that the emitting gas is generally clumpy in nature. Our assumption of $f = 1$ means that the calculated column densities are underestimates.

The radiation temperature, T_R , and the excitation temperature, T_{ex} , are related through

$$T_R = \frac{h\nu}{k} (1 - e^{-\tau_\nu}) \left(\frac{1}{e^{h\nu/kT_{ex}} - 1} - \frac{1}{e^{h\nu/kT_{bb}} - 1} \right) \quad (3)$$

where $h\nu$ is the energy of the transition (in our case $h\nu = \Delta E_{21}$), τ_ν is the optical depth at frequency ν , and the cosmic background radiation temperature, $T_{bb} = 2.7$ K. For the CO $J = 2 \rightarrow 1$ transition, $\Delta E_{21}/k = \Delta T_{21} = 11.06$ K. The effect of the cosmic background term is small and for the $J = 2 \rightarrow 1$ transition it may be considered negligible (less than 10%) provided $T_{ex} \geq 15$ K. Unless we are considering line ratios we drop this term. The radiation temperature becomes,

$$T_R = \Delta T_{21} \left(\frac{1 - e^{-\tau_\nu}}{e^{\Delta T_{21}/T_{ex}} - 1} \right) \quad (4)$$

If we assume that the line is optically thin at a given frequency ($\tau_\nu \ll 1$) the radiation temperature may be simplified even further to

$$T_R = \frac{\Delta T_{21} \tau_\nu}{e^{\Delta T_{21}/T_{ex}} - 1} \quad (5)$$

An estimate of the mass of the high-velocity gas may be determined using CO observations if we observe an optically thin transition (Lada, 1985). Although ^{12}CO emission is strongest and easiest to detect in flow sources, observations of ^{13}CO emission have shown that ^{12}CO emission is optically thick (i.e. $\tau^{12} > 1$) in most sources (Margulis & Lada, 1985). If we apply the radiation temperature equation (4) to both ^{12}CO and ^{13}CO we obtain the following relations:

$$T_R^{12}(2,1) = \Delta T^{12}(2,1) \left(\frac{1 - e^{-\tau^{12}}}{e^{\Delta T^{12}(2,1)/T_{ex}} - 1} \right), \quad (6)$$

$$T_R^{13}(2,1) = \Delta T^{13}(2,1) \left(\frac{1 - e^{-\tau^{13}}}{e^{\Delta T^{13}(2,1)/T_{ex}} - 1} \right). \quad (7)$$

If we assume the excitation temperatures for the ^{12}CO and ^{13}CO gas are the same (as with the beam filling factors) and that the isotopic abundance ratio, $R = N^{12}/N^{13}$, is known we can obtain τ^{12} , τ^{13} , and T_{ex} using the observed ratio T_R^{12}/T_R^{13} from the same transition (eg. $J = 2 \rightarrow 1$). This paper assumes an isotopic solar abundance ratio of $R = 89$, which implies that $\tau^{12} = 89 \cdot \tau^{13}$. $R = 89$ is an upper limit since some determinations give $R \approx 40$ to 60 . The observed ratio may therefore be expressed as

$$\frac{T_R^{12}(2,1)}{T_R^{13}(2,1)} = \frac{\Delta T^{12}(2,1) (1 - e^{-R\tau^{13}})}{\Delta T^{13}(2,1) (1 - e^{-\tau^{13}})} \left(\frac{\frac{1}{e^{\Delta T^{12}(2,1)/T_{ex}} - 1} - \frac{1}{e^{\Delta T^{12}(2,1)/T_{bb}} - 1}}{\frac{1}{e^{\Delta T^{13}(2,1)/T_{ex}} - 1} - \frac{1}{e^{\Delta T^{13}(2,1)/T_{bb}} - 1}} \right), \quad (8)$$

where $\Delta T^{13}(2,1) = 10.578\text{K}$ and $T_{bb} = 2.7\text{K}$. We then solve for τ^{13} at each channel for which ^{13}CO is detectable. Next, for each velocity interval described in Tables 2 and 3 we

take an average of the optical depth. We obtain τ^{12} from the relation, $\tau^{12} = 89 \cdot \tau^{13}$. In the velocity ranges where ^{13}CO is not detectable we assume that the ^{12}CO gas is optically thin.

For GL 490 we have only one ^{13}CO profile from which to determine τ^{12} so we must adopt the value obtained and use it over the entire mapped region. In the case of NGC 7538 IRS 9 we have ^{13}CO spectra at three offset positions, all of which are near the IR source. Since these positions are so close to each other we simply take an average of the three values obtained for τ^{12} and use this over the entire 20" map. For the central 10" map we use the value of τ^{12} obtained for the (0,0) offset.

Under the assumption of LTE, it follows from the solution for radiative transport that the optical depth for the $J = 2 \rightarrow 1$ transition is

$$\tau_\nu = \frac{c^2}{8\pi\nu^2} \frac{g_2}{g_1} A_{21} N_1 [1 - e^{-\Delta T_{21}/T_{ex}}], \quad (9)$$

where A_{21} is the rate of spontaneous radiative transition from $J = 2$ to $J = 1$ level, N_1 is the column density for the $J = 1$ rotational level, and g_1 and g_2 are statistical weights. By expressing A_{21} in terms of J_2 , integrating the optical depth, and using the relation, $d\nu/\nu = dv/v$, equation (9) becomes,

$$\int \tau(\nu) d\nu (\text{km}\cdot\text{s}^{-1}) = 1.5653 \times 10^{-15} \left(\frac{J_2}{2J_2 - 1} \right) N_{J=1} (1 - e^{-\Delta T_{21}/T_{ex}}), \quad (10)$$

where $J_2 = 2$ for the $J = 2 \rightarrow 1$ transition. We assume narrow, local profiles at each velocity channel and that $\int_{v_1}^{v_2} \tau(\nu) d\nu (\text{km}\cdot\text{s}^{-1})$ covers this local profile. v_1 and v_2 are the velocities at the opposite edges of a single channel. By integrating the radiation temperature in equation (5) and substituting equation (10) for $\int \tau(\nu) d\nu (\text{km}\cdot\text{s}^{-1})$ we can solve for the column density, $N_{J=1}$, of CO in the rotational level $J = 1$ at each channel by,

$$N_{J=1} = 8.67 \times 10^{13} e^{11.06/T_{ex}} \int T_R dv \text{ (km's}^{-1}\text{) cm}^{-2}. \quad (11)$$

This column density assumes the optically thin case.

If we assume Local Thermodynamic Equilibrium (LTE) then we may use the partition function, $Q = 2T_{ex}/\Delta T_{10}$ (Dickman, 1978), which is applied to obtain the total CO column density by $N_{CO} = Q \cdot N_{J=0}$ where $N_{J=0}$ is the column density of CO in rotational level $J = 0$. The relation between the column densities in the $J = 0$ and $J = 1$ rotational levels is

$$N_{J=0} = \frac{1}{3} e^{\Delta T (1,0)/T_{ex}} N_{J=1}, \quad (12)$$

where $\Delta T_{10} = 5.53\text{K}$. Therefore, the total CO column density is,

$$N_{CO} = \frac{1}{3} Q e^{5.53/T_{ex}} N_{J=1}, \quad (13)$$

and by substituting in for the partition function, Q , and for $N_{J=1}$, the total CO column density may then be expressed as,

$$N_{CO} = 1.05 \times 10^{13} T_{ex} e^{16.59/T_{ex}} \int T_R (2 \rightarrow 1) dv \text{ (km's}^{-1}\text{) cm}^{-2}. \quad (14)$$

Once we calculate N_{CO} for each velocity channel in a given velocity range we then sum them up and obtain N_{CO} for the given range. Since the CO column density derived in equation (14) uses the assumption that the gas is optically thin, we must make a correction for those velocity ranges where the ^{12}CO gas was found to be optically thick. A common practice is to multiply the column density by a correction factor $\tau^{12}/(1 - e^{-\tau^{12}})$. The

conversion factor is implied by comparing the radiation temperature for the optically thick case (eq. 4) to that of the optically thin case (eq. 5). After this is done we then sum up N_{CO} in each velocity range to obtain the total CO column density over the entire profile.

The total CO column density is related to the total H_2 column density by the conversion factor $X_{\text{CO}} = N_{\text{CO}}/N_{\text{H}_2} = 1.0 \times 10^{-4}$, which varies by a factor of ~ 2 throughout the Galaxy (Smith *et al.* 1991). We may now calculate the total H_2 mass found in the beam using the column density and the conversion factor with the relation for the mass in cell i of the map,

$$M_i(\text{H}_2) = N_i(\text{H}_2) \times m_i(\text{H}_2) \times A, \quad (15)$$

where $m_i(\text{H}_2)$ is the mass of diatomic hydrogen and A is the area of the beam in cm^2 at the source distance. In order to obtain the total mass of the outflow in the beam we must also take into account the fractional helium abundance of 10% by number. We then have the total mass in cell i of

$$M_i = 1.4 \times M_i(\text{H}_2). \quad (16)$$

The total mass over the entire map is then $M = \sum M_i$. Momentum and kinetic energy for cell i are represented by $p_i = \int m_i(v) v dv / \cos\theta$ and $E_i = \frac{1}{2} \int m_i(v) v^2 dv / \cos^2\theta$ where θ is the angle between the flow axis and the line-of-sight and we integrate over the entire velocity interval.

The dynamical timescale is defined as the length of time in which the gas has been outflowing. There is no generally accepted method, however, for determining this quantity. One of the most apparent drawbacks to any method is the lack of knowledge of

the flow orientation angle, θ . In this paper we discuss only the two most popular methods for determining the observed dynamical timescale of the outflows. The first method, described by Lada (1985), uses $t_1 = R_{\text{max}}/V_{\text{max}}$, where R_{max} is the maximum extent of the red (or blue) emission from the source and V_{max} is half of the total linewidth. The second commonly used method described by Cabrit and Bertout (1990) uses $t_2 = R_{\text{peak}}/\langle V \rangle$, where R_{peak} is the distance of the red (or blue) emission peak from the flow center and $\langle V \rangle$ is the mass weighted velocity given by $\langle V \rangle = P_{\text{tot}}/M_{\text{tot}} = \int m(v)v dv / \int m(v) dv$. These timescales will be used to calculate the mechanical luminosity, $L = E/t$, the mass flux, $\dot{M} = M/t$, and the momentum flux, $\dot{M}V$. The true timescale equals the observed timescale divided by $\tan\theta$, where, if $\theta < 45^\circ$, the observed timescales will be lower limits. The factor $\tan\theta$ arises from the angle between the outflow axis and the line of sight.

d) Uncertainties

The important uncertainties in our calculations and assumptions are given here. The small number of ^{13}CO observations in the ^{12}CO mapped regions leads to an uncertainty in the optical depth, τ^{12} . While the ^{13}CO profiles do not appear to change much over the mapped region the ^{12}CO profiles tend to vary drastically. Our use of an average τ^{12} over the entire map may lead to a large uncertainty in mass. However, we expect there to only be an uncertainty of a factor of 2 or 3 in mass since up to 50% of the total outflow mass is located in the region immediately surrounding the IR source where the ^{13}CO profiles are located. Also, most of the outflow mass is located in the optically thick part of the ^{12}CO wing which implies that the mass is approximately proportional to the assumed isotope ratio (ie. $M(\text{H}_2) \propto N(\text{H}_2) \propto N(^{12}\text{CO}) \propto \tau^{12} \propto R$ for opacity corrected mass). Our use of the solar isotope ratio gives an upper limit.

Another source of uncertainty lies in the source filling factor, f . The radiation temperature, and thus the integrated intensity, is directly proportional to the inverse of the filling factor. Our use of $f = 1$ gives a lower limit. If we assume CO $J = 2 \rightarrow 1$ is optically thin, however, then the effect of the beam filling factor on the total mass in the beam will be small (ie. $N \propto T_A^* / \eta f$ and $\text{mass} = N \times A'$, where A' = area filled by source. Since $A' = fA$, where A = area of beam, $\text{mass} = N \times fA = (T_A^* / \eta f) \times fA = T_A^* \times A / \eta$). The large degree of uncertainty in the excitation temperature does not greatly affect the mass due to the insensitivity of N_{CO} to T_{ex} . Column density and excitation temperature are related through $N_{\text{CO}} \propto T_{\text{ex}} \exp(16.59/T_{\text{ex}})$. If T_{ex} is in the range expected for GL 490 and NGC 7538 IRS 9 (ie. 20K to 35K) a difference of a factor of 2 or 3 in T_{ex} causes a 15-20% difference in N_{CO} . Our use of a single excitation temperature for each source has only a small effect on our results.

The orientation of the flow to the line-of-sight, θ , is, in general, not known. The momentum and kinetic energy depend on θ through $1/\cos\theta$ and $1/\cos^2\theta$ respectively. The amount of overlap between blue wing and red wing emission in GL 490 implies that θ is small and for NGC 7538 IRS 9 θ may be as large as 45° . The difference between $\theta = 0^\circ$ and $\theta = 45^\circ$ causes a difference of a factor of 1.4 in momentum and 2 in kinetic energy.

III. RESULTS

The shape of the line profile can give us information on some basic characteristics of the high-velocity gas as well as the quiescent gas. Noting how the profile changes across the mapped field may indicate such things as the presence of foreground or background clouds. This section gives a detailed description of the observed line profiles for GL 490 and NGC 7538 IRS 9 as well as their derived physical parameters (ie. mass, momentum, kinetic energy, etc.). By studying contour plots of integrated intensity as a function of velocity we can determine whether or not the outflows show a bipolar distribution. Acceleration or deceleration of an outflow can be inferred through a study of the position-velocity map of CO emission along the major axis of the outflow.

a) *GL 490*

Figures 4 and 5 show the $^{12}\text{CO } J = 2 \rightarrow 1$ spectral maps for the 20" and 10" spacing respectively. These two maps are combined in order to calculate column densities. A $^{13}\text{CO } J = 2 \rightarrow 1$ spectral line was obtained only for the (0,0) position. Figure 8 shows several $^{12}\text{CO } J = 2 \rightarrow 1$ spectra and the $^{13}\text{CO } J = 2 \rightarrow 1$ spectrum. The $^{12}\text{CO } J = 2 \rightarrow 1$ line wings at the position of GL 490 extend from $V_{\text{LSR}} = -50 \text{ km}\cdot\text{s}^{-1}$ to $+25 \text{ km}\cdot\text{s}^{-1}$ for a total line width of $75 \text{ km}\cdot\text{s}^{-1}$. Our observations of $^{13}\text{CO } J = 2 \rightarrow 1$ show a peak in emission at $V_{\text{LSR}} \approx -13.5 \text{ km}\cdot\text{s}^{-1}$ which is in good agreement with the result of $\sim -13 \text{ km}\cdot\text{s}^{-1}$ obtained by Lada & Harvey (1981) for $^{13}\text{CO } J = 1 \rightarrow 0$ and Snell *et al.* (1984) for $^{13}\text{CO } J = 2 \rightarrow 1$. The $-13.5 \text{ km}\cdot\text{s}^{-1}$ feature in the $^{12}\text{CO } J = 2 \rightarrow 1$ spectra reaches a peak antenna temperature of 20 K at GL 490 but drops to ~ 10 K at positions greater than 20" from the IR source. We can then adopt $V_0 = -13.5 \text{ km}\cdot\text{s}^{-1}$ for the central velocity, which appears to represent

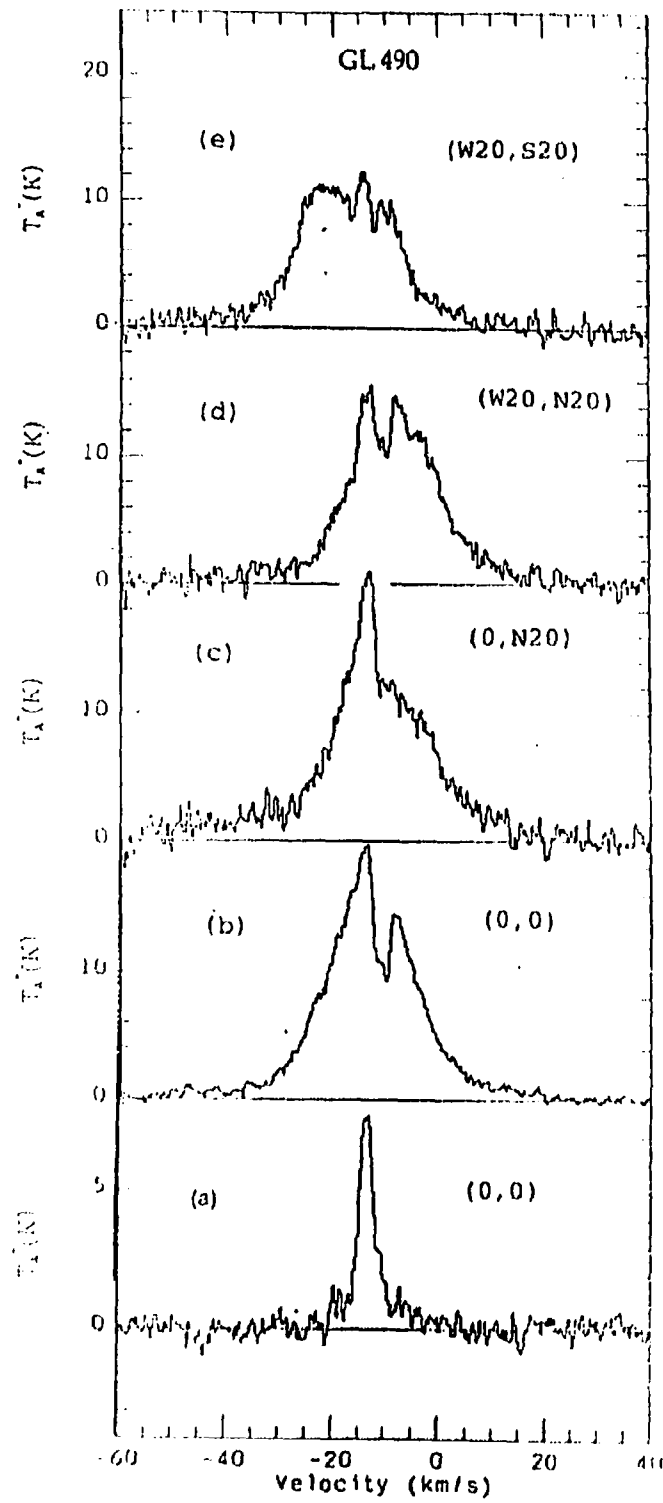


Figure 8. (a) The $^{13}\text{CO } J = 2 \rightarrow 1$ spectrum at GL 490. (b) -- (e) Selected ^{12}CO spectra. The map coordinates for each spectrum are given in arcseconds from GL 490. Note that the ^{13}CO spectrum temperature scale differs from that of the ^{12}CO spectra.

the velocity of the quiescent component of the GL 490 cloud. This component covers more than $1^\circ \times 1^\circ$ of sky (Snell *et al.*, 1984).

Our spectra clearly show a central dip $\sim 3 \text{ km}\cdot\text{s}^{-1}$ wide in the $^{12}\text{CO } J = 2 \rightarrow 1$ profile at the (0,0) position as well as at the (+20,0) and (+20,+20) positions. The dip is not evident in the data obtained by Lada & Harvey (1981) or Snell *et al.* (1984) due to their lower spatial resolution (48") and velocity resolution ($\Delta V_{\text{LSR}} \approx 2.6 \text{ km}\cdot\text{s}^{-1}$). Except for this dip, the ^{12}CO profile at the (0,0) position is symmetric about $V_0 = -13.5 \text{ km}\cdot\text{s}^{-1}$. This central dip (located from $-12 \text{ km}\cdot\text{s}^{-1}$ to $-9 \text{ km}\cdot\text{s}^{-1}$) may be due to foreground absorption by the quiescent cloud but this is not likely the cause since the ^{13}CO line peaks at $-13.5 \text{ km}\cdot\text{s}^{-1}$. There does, however, appear to be a "shoulder" to the ^{13}CO line at $-11 \text{ km}\cdot\text{s}^{-1}$ which may correspond to the ^{12}CO dip. Thus, another possible cause for the broad dip may be the blending of two separate absorptions, one at $-13.5 \text{ km}\cdot\text{s}^{-1}$ and the other at $-11 \text{ km}\cdot\text{s}^{-1}$. This is consistent with the shape of the spectra far from GL 490. The spectra in the outer regions of our mapped area show either a flat-topped or a double-peaked profile at $-13 \text{ km}\cdot\text{s}^{-1} \leq V_{\text{LSR}} \leq -8 \text{ km}\cdot\text{s}^{-1}$ which coincides with the central depression in the profile at GL 490. Lada & Harvey (1981) also show the ^{12}CO line core at $-14 \text{ km}\cdot\text{s}^{-1} \leq V_{\text{LSR}} \leq -10 \text{ km}\cdot\text{s}^{-1}$ using observations of $^{12}\text{CO } J = 1 \rightarrow 0$. The $-11 \text{ km}\cdot\text{s}^{-1}$ feature antenna temperature remains fairly constant at 8 -10 K whereas the $-13.5 \text{ km}\cdot\text{s}^{-1}$ feature peaks at GL 490. Two interpretations are possible: (1) the $-11 \text{ km}\cdot\text{s}^{-1}$ feature is due to an unrelated foreground gas cloud in the line of sight, or (2) it is due to a colder component in the outer regions of the GL 490 molecular cloud. The $-11 \text{ km}\cdot\text{s}^{-1}$ gas is seen as emission in both the ^{13}CO profile and at positions far from the IR source in the ^{12}CO line.

From an inspection of our $^{12}\text{CO } J = 2 \rightarrow 1$ profiles in the outer zones of the mapped region the quiescent component covers a velocity range of $-16 \text{ km}\cdot\text{s}^{-1}$ to $-8 \text{ km}\cdot\text{s}^{-1}$. There is a slight shift in the profile from one corner of the mapped region to the other causing an

uncertainty in the velocity range of $\sim 0.5 \text{ km}\cdot\text{s}^{-1}$. We, therefore, assume that the line core extends from $-16.5 \text{ km}\cdot\text{s}^{-1}$ to $-7.5 \text{ km}\cdot\text{s}^{-1}$. The wings in the $^{13}\text{CO } J = 2 \rightarrow 1$ profile extend from $\sim -22.0 \text{ km}\cdot\text{s}^{-1}$ to $\sim -3.0 \text{ km}\cdot\text{s}^{-1}$. Where the ^{13}CO wings are detectable, the optical depth in ^{12}CO is appreciable ($\tau^{12} \geq 1$). We separate the thick blue wing into two sections due to worries about contamination (from $-22.0 \text{ km}\cdot\text{s}^{-1}$ to $-18.5 \text{ km}\cdot\text{s}^{-1}$) possibly due to excess emission from a foreground or background cloud. The $-21.0 \text{ km}\cdot\text{s}^{-1}$ feature appears away from the central region of the mapped area, mostly to the south and east. For purposes of calculating column densities for the blueshifted gas we neglect the velocity range where the $-21.0 \text{ km}\cdot\text{s}^{-1}$ contamination is prominent. Using the above criteria we divide the ^{12}CO profile into the velocity ranges outlined in Table 2. The optical depths, which are calculated from the $^{12}\text{T}_R/^{13}\text{T}_R$ ratio, are also listed in this table and are in fairly good agreement with Snell *et al.* (1984).

From channel maps made in various velocity ranges (Fig. 9) we may determine the distribution of the redshifted and blueshifted gas. Antenna temperature is integrated over velocity channels of width $10 \text{ km}\cdot\text{s}^{-1}$. The redshifted gas (seen in the 4 panels from $-10 \text{ km}\cdot\text{s}^{-1}$ to $30 \text{ km}\cdot\text{s}^{-1}$ in Fig. 9) exhibits an elongated distribution extending $\sim 30''$ north in the east-west direction while the main red peak lies $\sim 20''$ to the north-northwest. The blueshifted gas (seen in the 4 panels from $-10 \text{ km}\cdot\text{s}^{-1}$ to $-50 \text{ km}\cdot\text{s}^{-1}$ in Fig. 9) tends to show more of a circular distribution which peaks southwest ($-10, +30$) of GL 490. A map of the blue and redshifted gas superimposed on each other is shown in Figure 10. Since the results obtained by Snell *et al.* (1984) are qualitatively similar to our observations we will compare the two. Some of the notable differences lie in the separation between blue and red peaks and the location of the centroid with respect to the IR source. Snell *et al.* (1984) find a separation of $30''$ along a north-south line with the centroid located $34''$ southwest of GL 490 while our results show a separation of $\sim 40''$ with the centroid located $18''$ west of the IR source. This displacement of the apparent centroid from the IR source is not a cause

TABLE 2
VELOCITY RANGES FOR ^{12}CO PROFILES IN GL 490

Velocity Range (in $\text{km}\cdot\text{s}^{-1}$)	Description	Optical Depth
-50.0 to -40.0	outer blue wing	<1
-40.0 to -30.0	thin blue wing	<1
-30.0 to -22.0	strong blue wing	<1
-22.0 to -18.5	thick blue wing (contaminated?)	3.7
-18.5 to -16.5	thick blue wing (uncontaminated)	6.8
-16.5 to -7.5	line core (or quiescent gas)	>>1
-7.5 to -3.0	thick red wing	6.2
-3.0 to +5.0	strong red wing	4.0
+5.0 to +15.0	thin red wing	<1
+15.0 to +25.0	outer red wing	<1

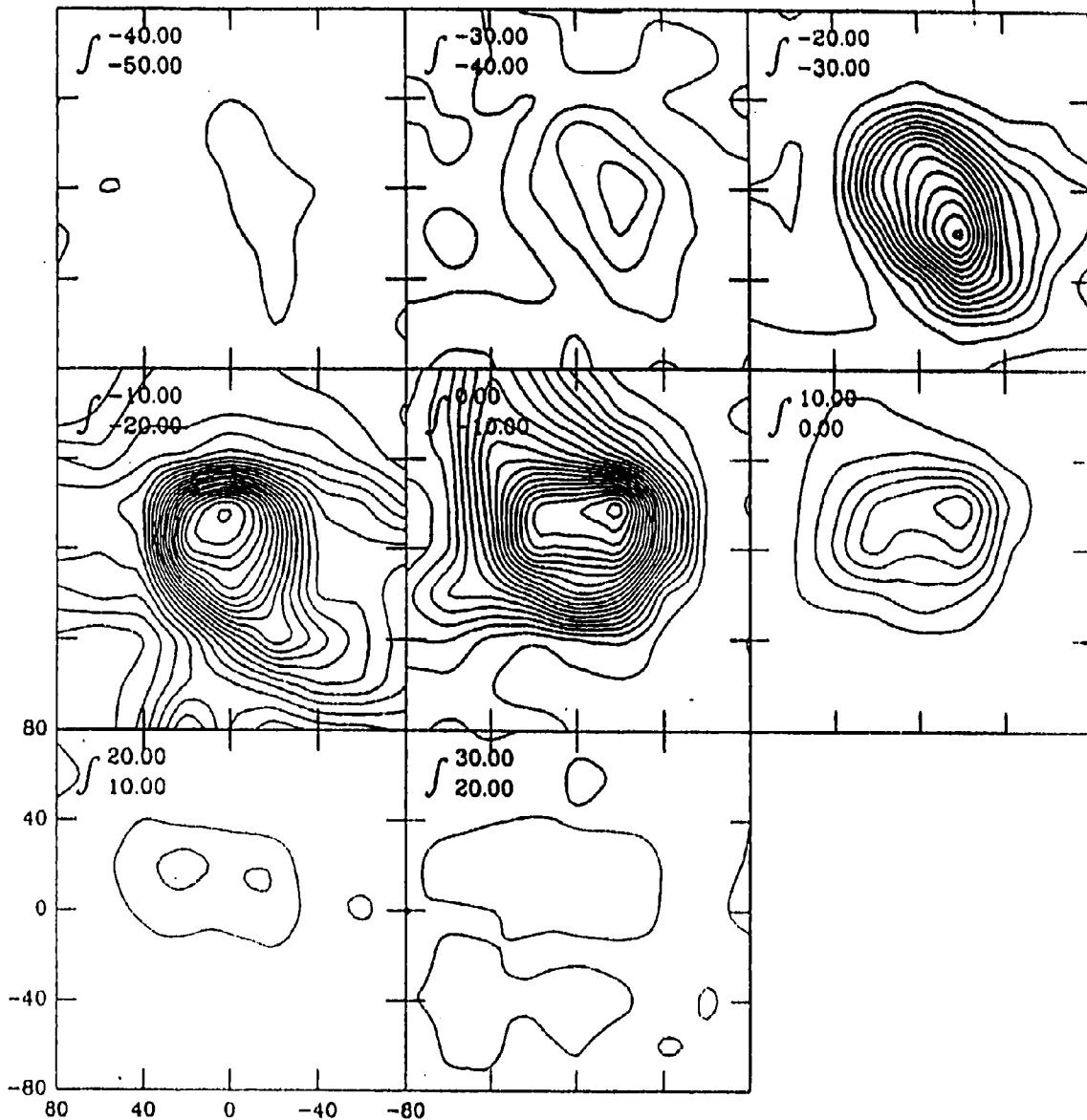


Figure 9. Channel maps of GL 490 showing the changing spatial distribution of CO emission as a function of velocity. Antenna temperature is integrated over channels of width $10 \text{ km}\cdot\text{s}^{-1}$. The base level is $0 \text{ K}\cdot\text{km}\cdot\text{s}^{-1}$ and the contour interval is $5 \text{ K}\cdot\text{km}\cdot\text{s}^{-1}$.

for alarm. Since the redshifted emission is elongated to the west there is some doubt as to the position of the emission peak. With this in mind we use the major axis of the outer contours in Figure 10 which passes through GL 490. This is indicative of GL 490 being the source of the outflow.

Determining the position of the high-velocity emission as a function of velocity in the line wings can provide information about whether the stellar outflow is interacting with the ambient cloud, either at the end of the flow or continuously along its length (Snell *et al.*, 1984). In the graph showing the changing position of the emission peak with velocity for GL 490 (see Figure 11) we note that the blue and redshifted high-velocity emission centroids tend to be located on opposite sides of the peak corresponding to the line center emission. This is to be expected for a bipolar outflow. The position of the velocity-dependent red emission peak wanders at velocities near the line center and may be due to the presence of the self-absorption feature. There also appears to be a systematic shift in position of the red wing emission centroid away from the IR source with velocities increasing redward from $12 \text{ km}\cdot\text{s}^{-1}$. Acceleration of the outflow may cause this shift. The emission peak at $-13.5 \text{ km}\cdot\text{s}^{-1}$ (the line center) is offset from the IR source. The offset may be explained if the IR source is not located at the center of the cloud core. The blue wing of emission centroids tend to cluster at two different locations, $(-20,0)$ for velocities greater than $-30 \text{ km}\cdot\text{s}^{-1}$ and at $(-20,-20)$ for velocities between -20 and $-25 \text{ km}\cdot\text{s}^{-1}$. Snell *et al.* (1984), in a similar figure, find that a clump of points near $(-20,-20)$ could be related to the $-21 \text{ km}\cdot\text{s}^{-1}$ feature and may indicate that this feature should be considered separately. Since the $-21 \text{ km}\cdot\text{s}^{-1}$ feature is quite weak, however, compared to the blue wing emission and probably does not affect the results greatly, we assume this clumping of points to be real and a part of the GL 490 outflow. The complexity of Figure 11 may indicate an interaction between the outflow and the ambient gas all along the length of the outflow.

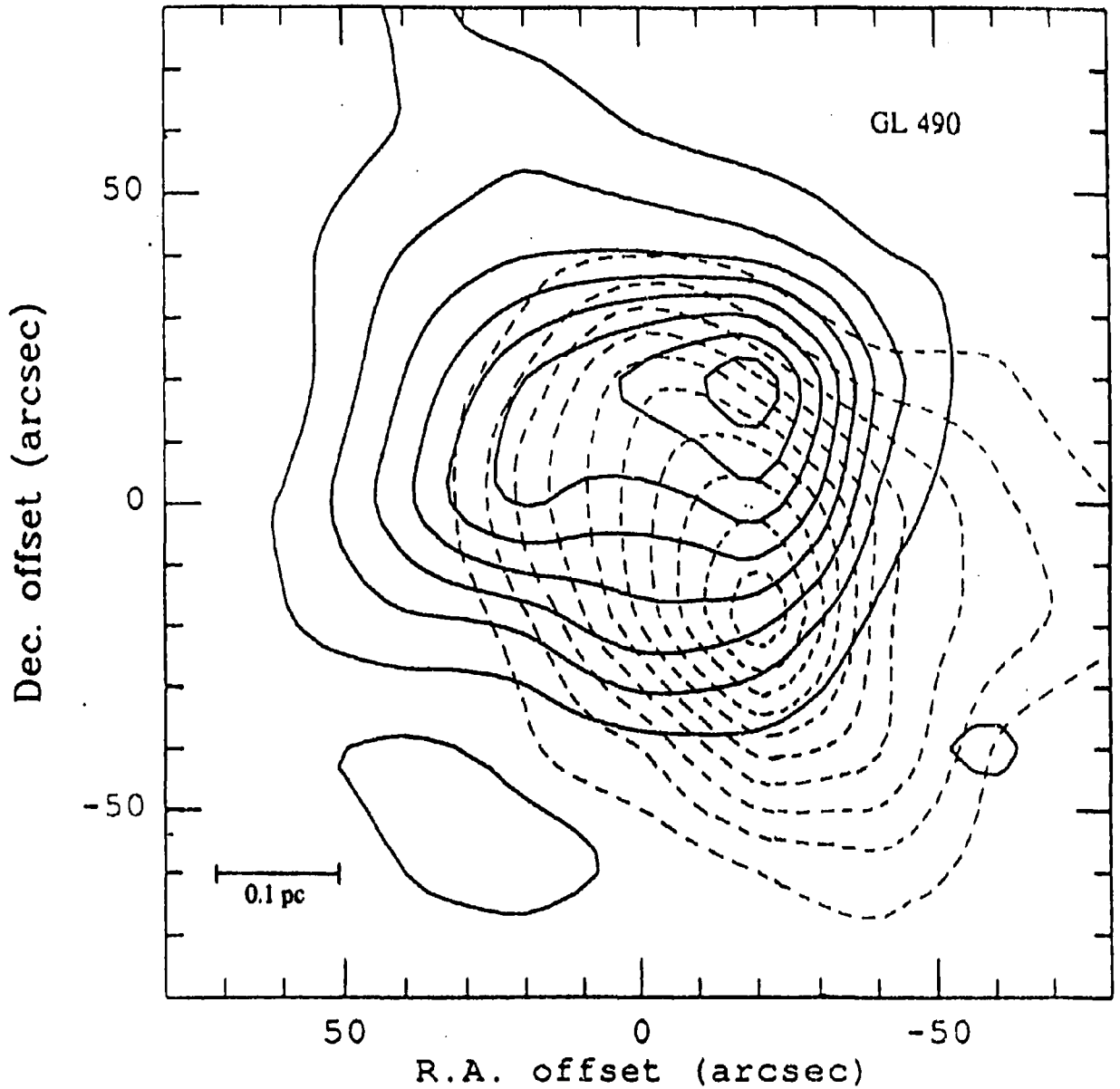


Figure 10. Integrated intensity in the red and blue wing CO $J = 2 \rightarrow 1$ emission from GL 490. Red wing emission (solid lines) includes velocities from 0 to 5 $\text{km}\cdot\text{s}^{-1}$, with a minimum contour of 0 $\text{K}\cdot\text{km}\cdot\text{s}^{-1}$ and a contour interval of 2.5 $\text{K}\cdot\text{km}\cdot\text{s}^{-1}$. The blue wing emission (dashed lines) includes velocities from -30 to -25 $\text{km}\cdot\text{s}^{-1}$, with a minimum contour of 0 $\text{K}\cdot\text{km}\cdot\text{s}^{-1}$ and a contour interval of 2.5 $\text{K}\cdot\text{km}\cdot\text{s}^{-1}$.

GL 490
CO J = 2→1
EMISSION CENTROID

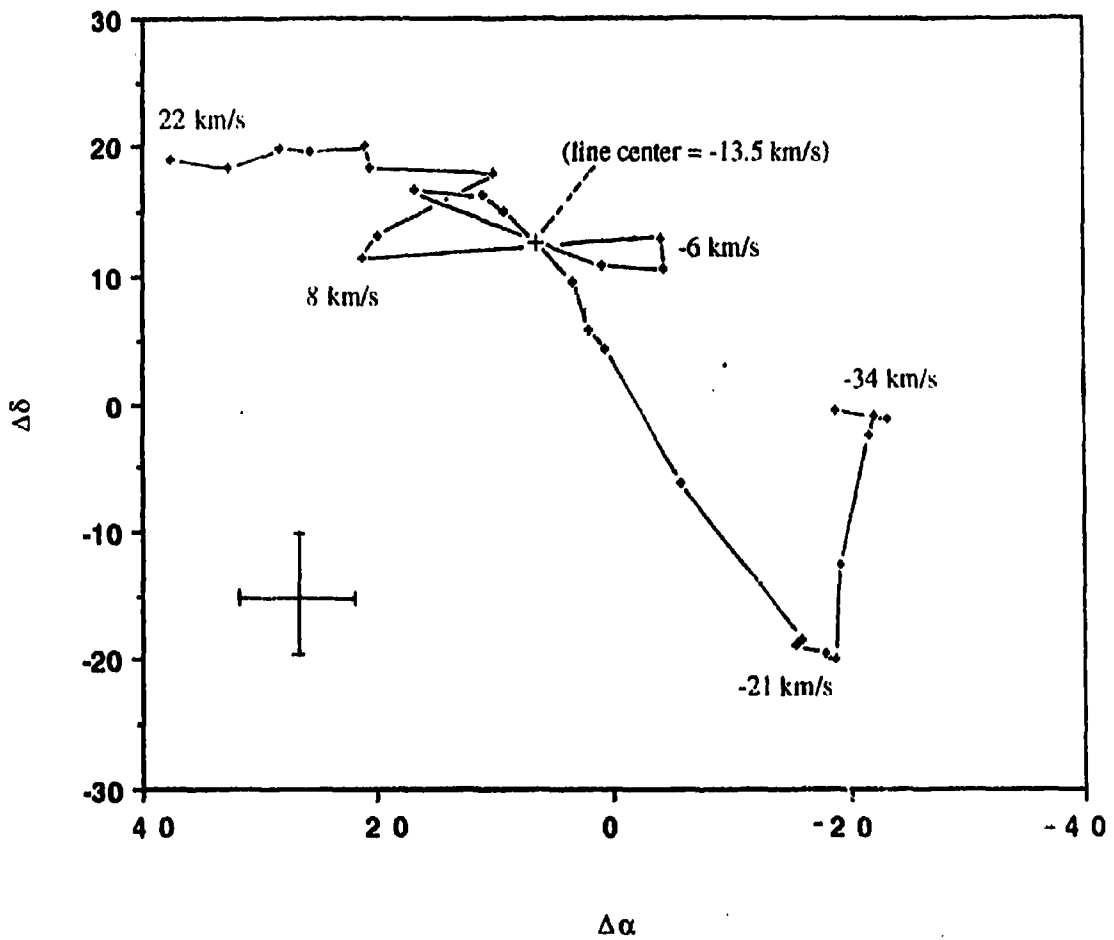


Figure 11. The location of the emission centroid as a function of velocity for the CO J = 2→1 emission in GL 490. The position offsets are relative to the position of the IR source. The point representing the peak intensity is indicated by a plus symbol. The error in position is taken to be half the beamwidth (ie. ~10").

The position-velocity map of CO emission, along a line with constant right ascension ($\Delta\alpha = -20''$), for GL 490 (Fig. 12) shows that the velocity field of the molecular outflow extends away from that of the ambient gas indicating that the velocity field of the molecular outflow is distinct from that of the ambient cloud. The blueshifted gas has two components: a weak intensity peak at $\sim -32 \text{ km}\cdot\text{s}^{-1}$ near the IR source and a stronger peak at $\sim -17 \text{ km}\cdot\text{s}^{-1}$ roughly $40''$ south of the source. The redshifted gas displays only one intensity peak at $\sim -7 \text{ km}\cdot\text{s}^{-1}$ located $20''$ north of GL 490. A multicomponent nature such as that shown for the blue lobe may indicate shell structure (Wolf *et al.* 1990). A deceleration of the outflow is indicated since red and blueshifted velocities are higher toward the flow center and decrease with increasing distance from the source. Figure 12 also shows that the red and blueshifted lobes overlap spatially. These results are consistent with position-velocity maps created by Cabrit & Bertout (1990) for a decelerated outflow whose opening angle, θ_{max} , is greater than the inclination angle of the flow to the line of sight, θ . The acceleration of the outflow for velocities greater than $12 \text{ km}\cdot\text{s}^{-1}$ seen in Figure 11 is not evident in the position-velocity map since Figure 12 does not include the region where the outer red wing is prominent.

Upon examination of the high S/N spectra in the 3×3 map using $10''$ spacing there appears to be two distinct features in the outer blue wing. Although the individual spectra do not exhibit these features conclusively, an average of the 9 high S/N spectra clearly shows a feature at $-46 \text{ km}\cdot\text{s}^{-1}$ and at $-42 \text{ km}\cdot\text{s}^{-1}$. As can be seen in Figure 13, these features are $3\text{-}4 \text{ km}\cdot\text{s}^{-1}$ in width and display a non-gaussian shape. The two most plausible explanations for these features may be, (1) that they are due to gas in the line of sight, or (2) that they represent velocity structure in the flow itself. If we believe the second explanation we may visualize the two features as being two discrete clumps of material ejected from GL 490. High resolution observations in a second transition would help to clarify this matter.

POSITION-VELOCITY MAP FOR GL 490

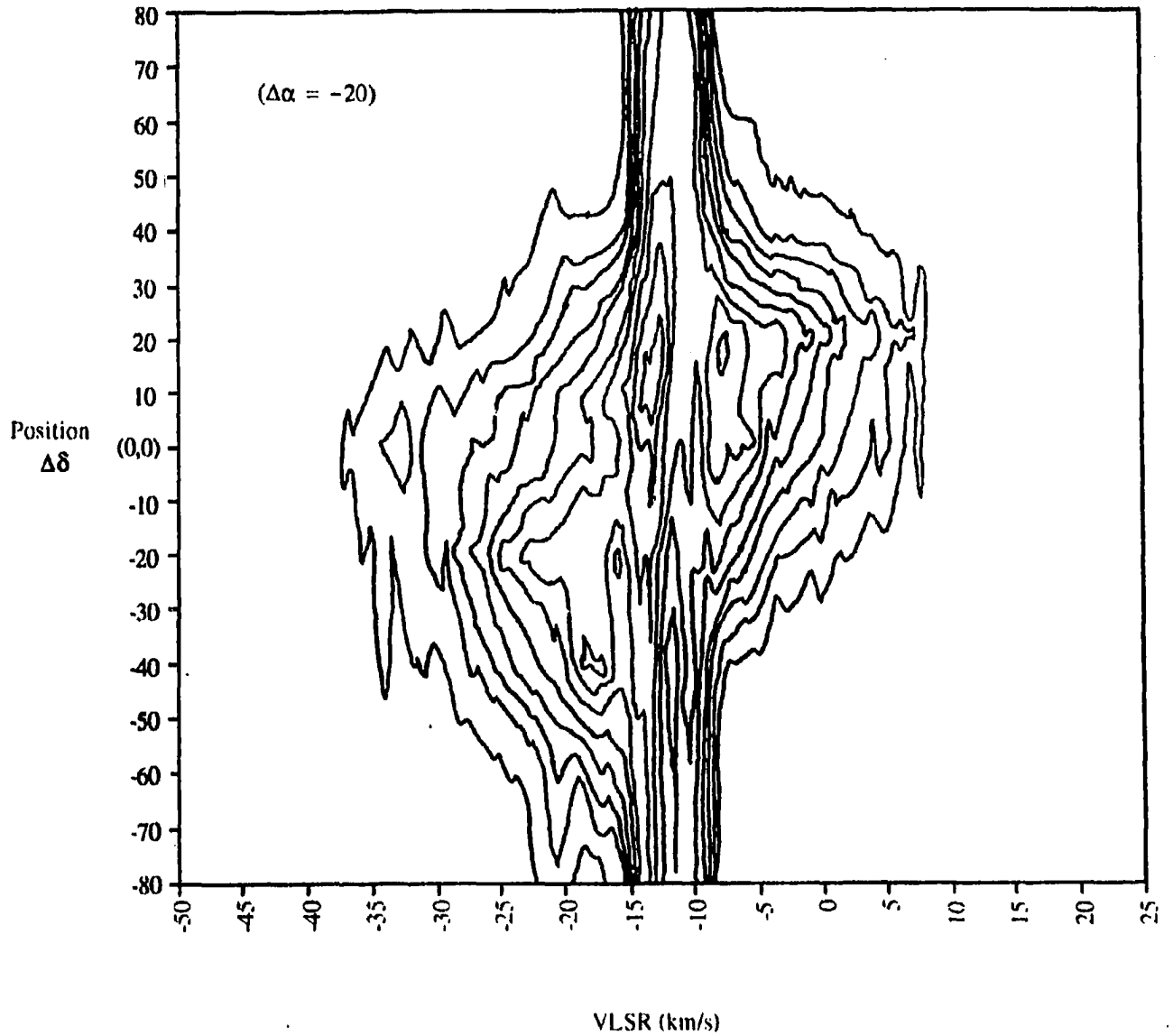


Figure 12. Position-velocity map of CO emission along a line of constant right ascension ($\Delta\alpha = -20''$) for GL 490. The minimum contour is $8 \text{ K}\cdot\text{km}\cdot\text{s}^{-1}$ with a contour interval of $8 \text{ K}\cdot\text{km}\cdot\text{s}^{-1}$.

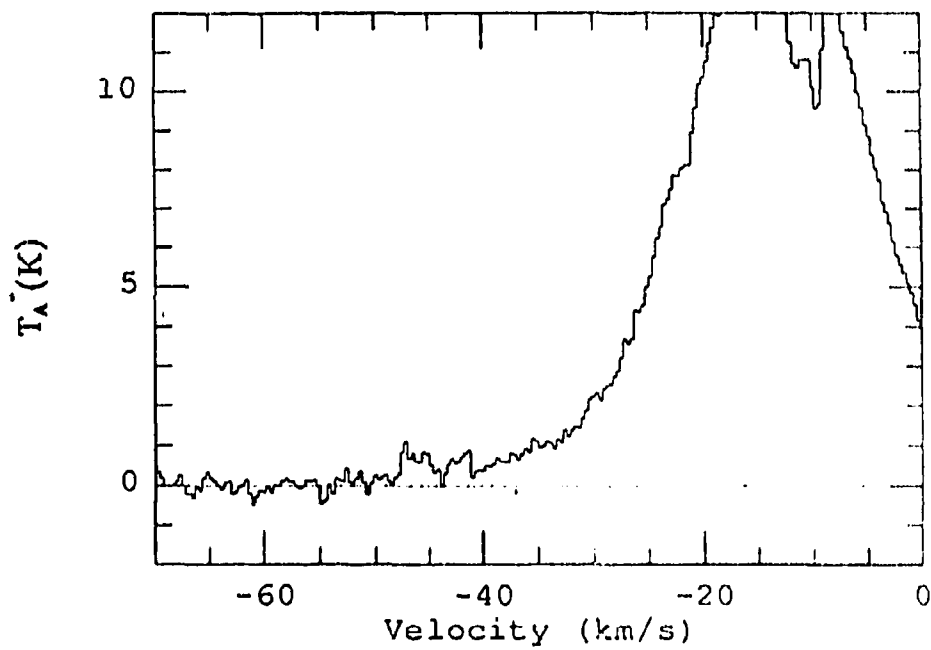


Figure 13. A $^{12}\text{CO } J = 2 \rightarrow 1$ spectrum of GL 490 showing velocity structure in the blue wing. The spectrum is an average of the 9 spectra in a 3×3 map with $10''$ spacing, centered on GL 490.

From equation (6) we may calculate the CO excitation temperature (assuming $f = 1$). Our results show that $T_{\text{ex}} = 15 - 25$ K throughout the inner wings. We therefore adopt a value of $T_{\text{ex}} = 20$ K with which we calculate the outflow properties for GL 490, as described in section §2c. These results are shown in Tables 4 and 5. Snell *et al.* (1984) obtain similar results where they use $T_{\text{ex}} \approx 15$ K for the wings and $T_{\text{ex}} \approx 25$ K for the quiescent gas. Using both methods described in §2c to calculate the dynamical timescale we obtain ages of $t_1 = R_{\text{max}}/V_{\text{max}} = 11,300$ years and $t_2 = R_{\text{peak}}/\langle V \rangle = 10,700$ years. The outflow mass for the blueshifted gas was found to be $3.9 M_{\odot}$ while that of the redshifted gas was $4.8 M_{\odot}$ giving a total outflow mass of $8.7 M_{\odot}$. The total outflow momentum and kinetic energy were calculated to be $\sim 74 M_{\odot} \text{ km/s}$ and 8.3×10^{45} ergs respectively. Dividing kinetic energy by dynamical timescale (t_1 and t_2 separately) we obtain mechanical luminosities, $L_1 = 6.8 L_{\odot}$ and $L_2 = 6.5 L_{\odot}$. The corresponding mass loss rates are $\dot{M}_1 = 8.2 \times 10^{-4} M_{\odot}/\text{yr}$ and $\dot{M}_2 = 5.9 \times 10^{-4} M_{\odot}/\text{yr}$.

b) *NGC 7538 IRS 9*

The $^{12}\text{CO } J = 2 \rightarrow 1$ spectral data consists of a 7×7 map using $20''$ spacing (shown in Fig. 6) and a 3×3 map using $10''$ spacing and a higher S/N (see Fig. 7). $^{13}\text{CO } J = 2 \rightarrow 1$ spectral data were obtained for three positions close to NGC 7538 IRS 9. Figure 14 shows the $^{13}\text{CO } J = 2 \rightarrow 1$ spectra with the corresponding $^{12}\text{CO } J = 2 \rightarrow 1$ spectra shifted 2 K for clarity. In observations of $^{12}\text{CO } J = 1 \rightarrow 0$, Kameya *et al.* (1989) found that the line peak corresponded to a $V_{\text{LSR}} \approx -58 \text{ km}\cdot\text{s}^{-1} \pm 1 \text{ km}\cdot\text{s}^{-1}$ for IRS 9. The $-58 \text{ km}\cdot\text{s}^{-1}$ line peak represents the quiescent component. A second peak in the $^{12}\text{CO } J = 1 \rightarrow 0$ transition at $V_{\text{LSR}} \approx -49 \text{ km}\cdot\text{s}^{-1}$ is evident all over the IRS 9 and IRS 11 regions and may be due to an independent foreground cloud. In our data for $^{12}\text{CO } J = 2 \rightarrow 1$ and $^{13}\text{CO } J = 2 \rightarrow 1$ the $-49 \text{ km}\cdot\text{s}^{-1}$ secondary peak can also be seen, though it is shifted slightly blueward for ^{12}CO (possibly due to some off position emission encountered during on-off position switching, Mitchell & Hasegawa, 1991). Another possibility may be due to a small AOSC velocity uncertainty of $\pm 0.5 \text{ km}\cdot\text{s}^{-1}$. The $-49 \text{ km}\cdot\text{s}^{-1}$ feature has a fairly constant antenna temperature of 8 - 10 K over the entire mapped region.

The main peak for the $^{13}\text{CO } J = 2 \rightarrow 1$ data appears at $V_{\text{LSR}} \approx -57.5 \text{ km}\cdot\text{s}^{-1} \pm 0.5 \text{ km}\cdot\text{s}^{-1}$ (the error is due to a slight shifting of the peak from $-57 \text{ km}\cdot\text{s}^{-1}$ at E00N20 to $-58 \text{ km}\cdot\text{s}^{-1}$ at E20S40). The $-57.5 \text{ km}\cdot\text{s}^{-1}$ peak corresponds to the main peak for the quiescent component found in $^{12}\text{CO } J = 1 \rightarrow 0$ (Kameya *et al.*, 1989). $^{12}\text{CO } J = 2 \rightarrow 1$ displays a fairly prominent peak at $\sim -60 \text{ km}\cdot\text{s}^{-1}$ which does not have a ^{13}CO counterpart. The $-60 \text{ km}\cdot\text{s}^{-1}$ peak may be a slightly warmer gas with a smaller optical depth. We adopt the ^{13}CO peak of $-57.5 \text{ km}\cdot\text{s}^{-1}$ as the central velocity of the IRS 9 cloud, since it agrees with the $^{12}\text{CO } J = 1 \rightarrow 0$ data. There is, however, a slight shoulder in the $^{13}\text{CO } J = 2 \rightarrow 1$ spectra at $-60 \text{ km}\cdot\text{s}^{-1}$ which may be related to the $-60 \text{ km}\cdot\text{s}^{-1}$, $^{12}\text{CO } J = 2 \rightarrow 1$ feature. The $^{12}\text{CO } J = 2 \rightarrow 1$ line wing at the position of IRS 9 extends from $V_{\text{LSR}} = -90 \text{ km}\cdot\text{s}^{-1}$ to

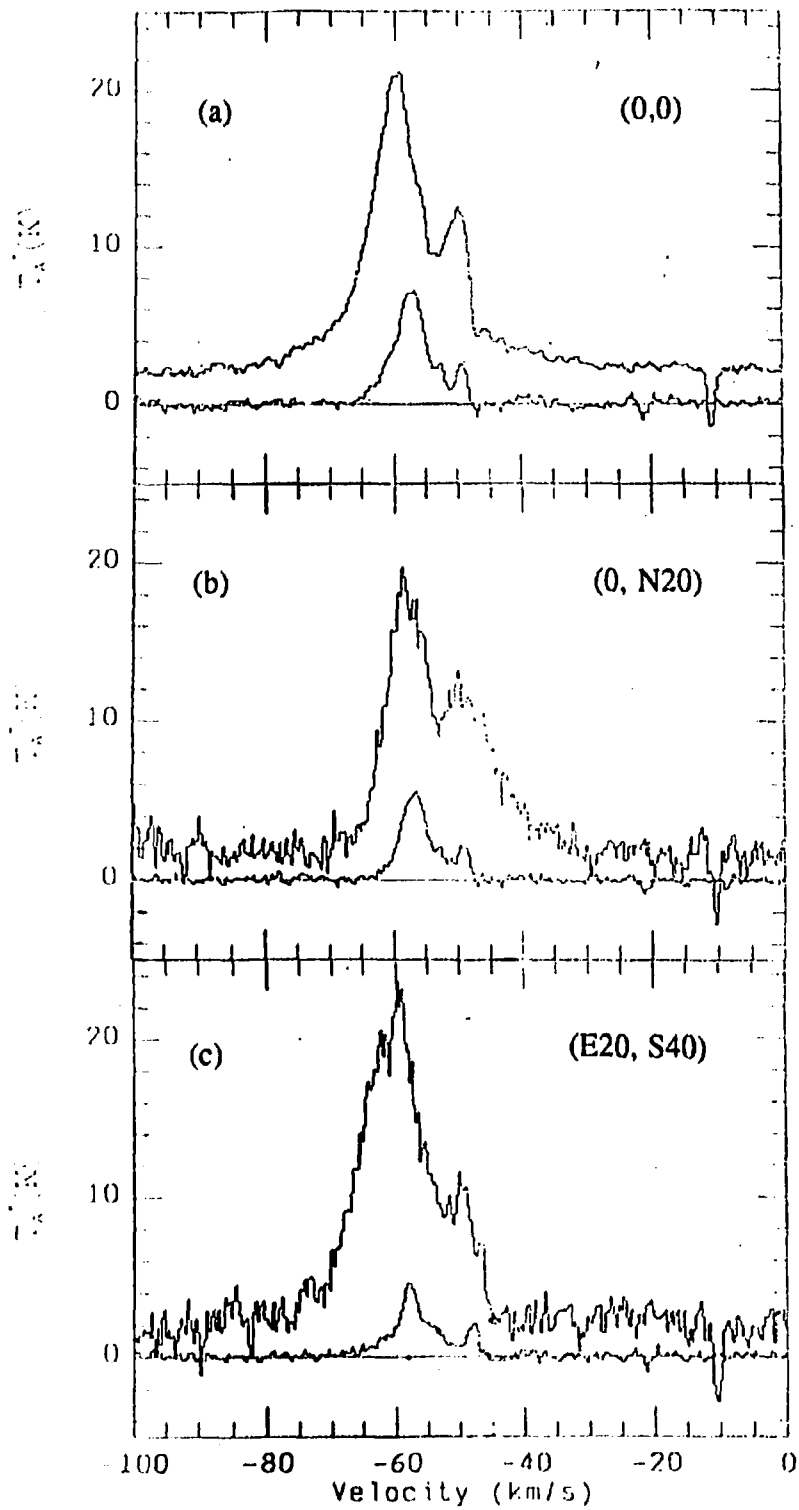


Figure 14. (a) - (c) The $^{12}\text{CO } J = 2 \rightarrow 1$ and $^{13}\text{CO } J = 2 \rightarrow 1$ spectra for NGC 7538 IRS 9. The map coordinates for each spectrum are given in arcseconds from NGC 7538 IRS 9. Note that the ^{12}CO spectra is shifted 2 K from the ^{13}CO spectra.

-22 km·s⁻¹, for a total line width of 68 km·s⁻¹. There may be a weak red wing extending out to ~0 km·s⁻¹ which is not used since the off source position used for the ¹²CO observations contained emission at $V_{LSR} = -10$ km·s⁻¹ appearing as an absorption feature in the red wing (see Fig. 14). The main peak has an antenna temperature which changes from ~10 K in the outer regions of the map to 20 - 21 K near the IR source.

By examining the ¹²CO J = 2→1 profiles near the perimeter of the mapped region we note that the quiescent component seems to cover the range from -47 km·s⁻¹ to -60 km·s⁻¹ although, due to the presence of the secondary peak, the red wing appears to be contaminated in the velocity range $-55 \text{ km}\cdot\text{s}^{-1} \leq V_{LSR} \leq -47 \text{ km}\cdot\text{s}^{-1}$. The blue wing is not contaminated. The ¹³CO J = 2→1 profile is detectable for $-67 \text{ km}\cdot\text{s}^{-1} \leq V_{LSR} \leq -47 \text{ km}\cdot\text{s}^{-1}$. In this region we assume the ¹²CO line is optically thick. Using the above criteria we then divide the ¹²CO J = 2→1 profile into the sections outlined in Table 3 below, along with the relative optical depths (calculated from the ¹²T_R/¹³T_R ratio).

Using the channel maps made from various velocity ranges (Fig. 15), we obtain information concerning the distribution of the red and blueshifted gas. The shape and position of the main blueshifted emission peak at (20",-30") remains constant with changing velocity in the blue wing, suggesting a well defined cone of emission. The redshifted gas, however, shows one main peak of emission at (0,20") which remains fairly constant in position and shape throughout the red wing. A smaller emission peak shows up from -46 km·s⁻¹ to -48 km·s⁻¹ at the (0,-20") position and another one from -40 km·s⁻¹ to -46 km·s⁻¹ at the (0,-40") position. These "clumps" may indicate that a simple biconical outflow model does not apply in this case. Kameya *et al.* (1989) found the distribution of the outflow gas to be quite complex with the blueshifted gas being situated southeast of IRS 9 and the redshifted gas was situated to the north, east, and southwest of the IR source. We can not rely heavily on their results, however, since they only use

TABLE 3

VELOCITY RANGES FOR ^{12}CO PROFILES IN NGC 7538 IRS 9

Velocity Range ($\text{km}\cdot\text{s}^{-1}$)	Description	Optical Depth
-87.0 to -77.0	outer blue wing	<1
-77.0 to -67.0	thin blue wing	<1
-67.0 to -60.0	thick blue wing	8.2
-60.0 to -55.0	line core (or quiescent gas)	>>1
-55.0 to -52.0	mixed component (contaminated)	---
-52.0 to -47.0	second component (contaminated)	---
-47.0 to -37.0	thin red wing	<1
-37.0 to -27.0	outer red wing	<1

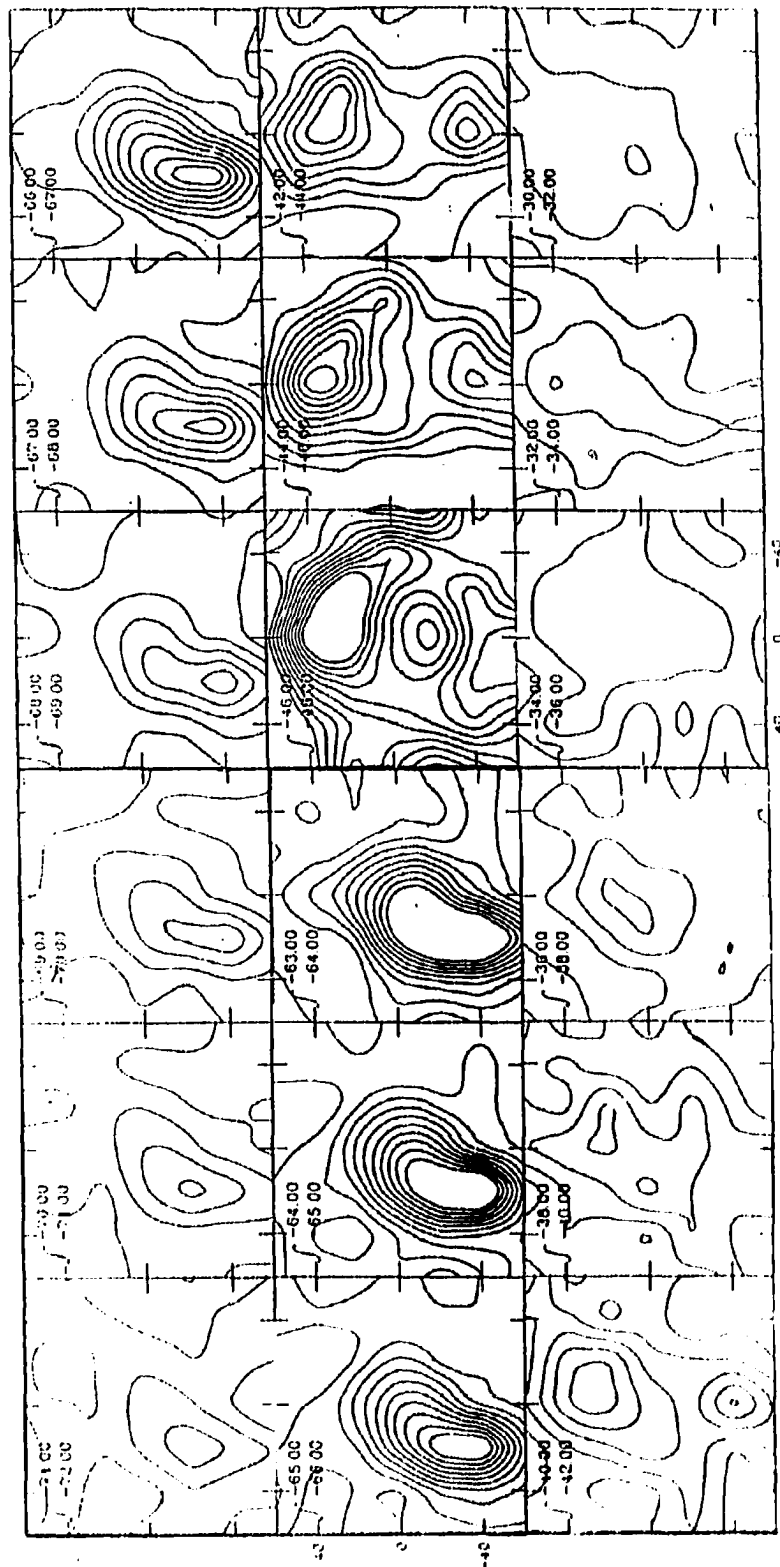


Figure 15. Channel maps of NGC 7538 IRS 9 showing the changing spatial distribution of CO emission as a function of velocity. Antenna temperature is integrated over channels of width $2 \text{ km}\cdot\text{s}^{-1}$ for the redshifted flow and width $1 \text{ km}\cdot\text{s}^{-1}$ for the blueshifted flow. The base level is $0 \text{ K}\cdot\text{km}\cdot\text{s}^{-1}$ and the contour interval is $1 \text{ K}\cdot\text{km}\cdot\text{s}^{-1}$. A gap in the maps from -48 to $-63 \text{ km}\cdot\text{s}^{-1}$ was made to exclude the line core and mixed component. The separation of the tick marks on the abscissa is $40''$.

observations in a single transition, CO J = 1→0, in which the wings are barely detectable. They found a general bipolar nature to the outflow. Our data shows this bipolarity clearly. As we see in Figure 16, there is a separation between the red and blueshifted emission peaks of ~70". The redshifted gas distribution is slightly elongated, extending ~20" to the southwest of the emission peak which is centered 30" north of IRS 9. The blueshifted gas also has an elongated distribution, extending ~30" north of the emission peak which lies 40" to the southeast of IRS 9. The center of the line connecting the red and blue emission peaks lies only 8" east of the IR source. This displacement from the IR source is small enough so that we may be confident that NGC 7538 IRS 9 is the source of the outflow.

Figure 17 shows a graph of the changing position of the emission peak with velocity. Unlike GL 490, the red and blue high-velocity emission peaks are separated into two distinct clusters ~70" apart with no evidence of a systematic shift in the position of the red and blue wing emission. The position of the peak of the line center emission lies closer to the blueshifted gas. The emission peak at $-58.5 \text{ km}\cdot\text{s}^{-1}$ (the line center) is offset from the IR source. The offset is similar to the case in GL 490 implying that the IR source is not located at the center of the cloud core. Since the emission peaks lie in two distinct clumps on opposite sides of the position for the line center, this suggests a model in which the outflow interacts with the ambient gas mostly at the end of the jet (Snell *et al.*, 1984).

In the position-velocity diagram of CO emission along the major axis of the NGC 7538 IRS 9 outflow (Fig. 18) there is evidence that the velocity field of the molecular outflow is distinct from that of the ambient gas. The lack of multiple components in the red and blue lobes implies that shell structure is not resolved. The red and blue lobes do not overlap spatially by a great amount implying that the flow opening angle, θ_{max} , is not

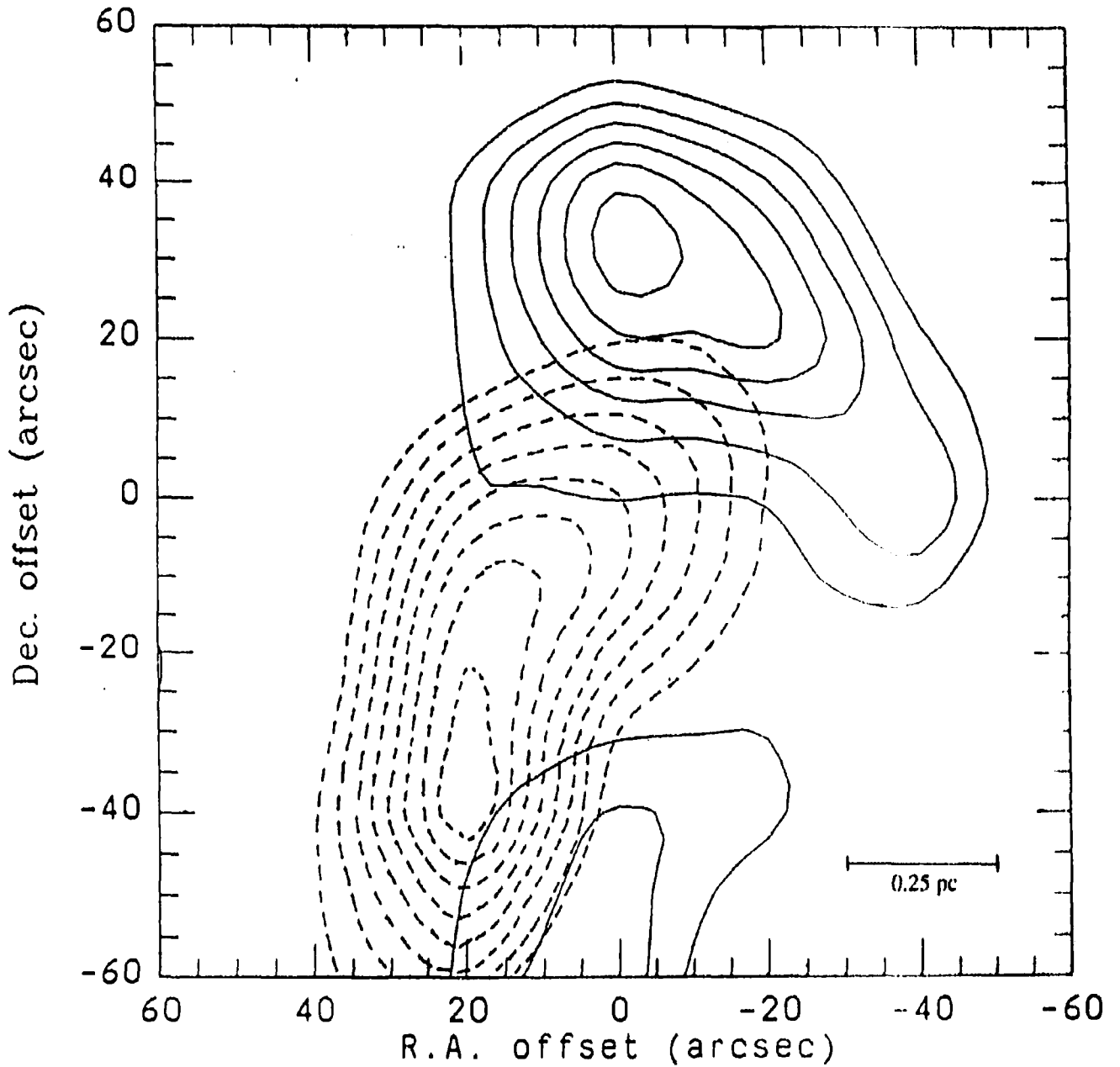


Figure 16. Integrated intensity in the red and blue wing CO $J = 2 \rightarrow 1$ emission from NGC 7538 IRS 9. Red wing emission (solid lines) includes velocities from -47 to $-44 \text{ km}\cdot\text{s}^{-1}$, with a maximum contour of $17 \text{ K}\cdot\text{km}\cdot\text{s}^{-1}$ and a contour interval of $2 \text{ K}\cdot\text{km}\cdot\text{s}^{-1}$. The blue wing emission (dashed lines) includes velocities from -71 to $-68 \text{ km}\cdot\text{s}^{-1}$, with a maximum contour of $11 \text{ K}\cdot\text{km}\cdot\text{s}^{-1}$ and a contour interval of $1 \text{ K}\cdot\text{km}\cdot\text{s}^{-1}$.

NGC 7538 IRS 9
CO J = 2→1
EMISSION CENTROID

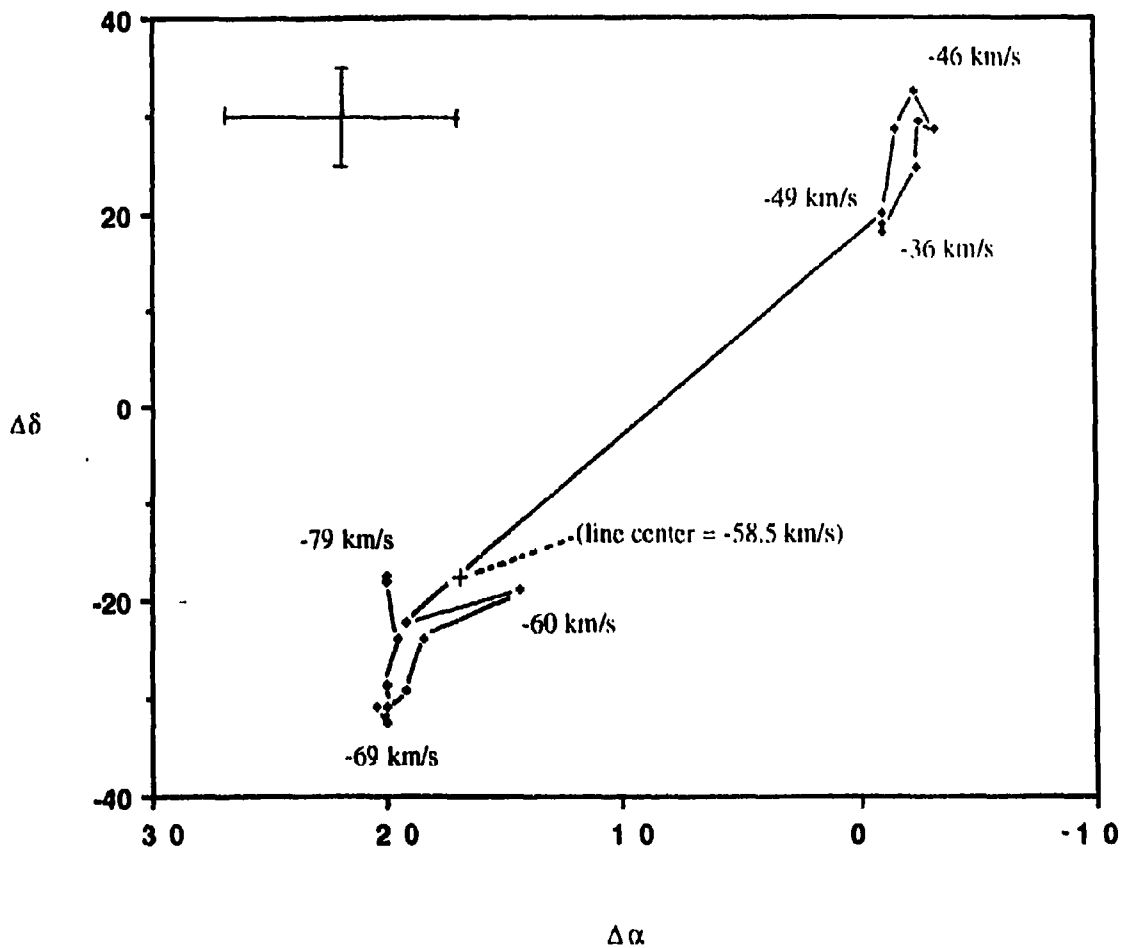


Figure 17. The location of the emission centroid as a function of velocity for the CO J = 2→1 emission in NGC 7538 IRS 9. The position offsets are relative to the position of the IR source. The point representing the peak intensity is indicated by a plus symbol. The error in position is taken to be half the beamwidth (i.e. $\sim 10''$).

POSITION-VELOCITY MAP FOR NGC 7538 IRS 9

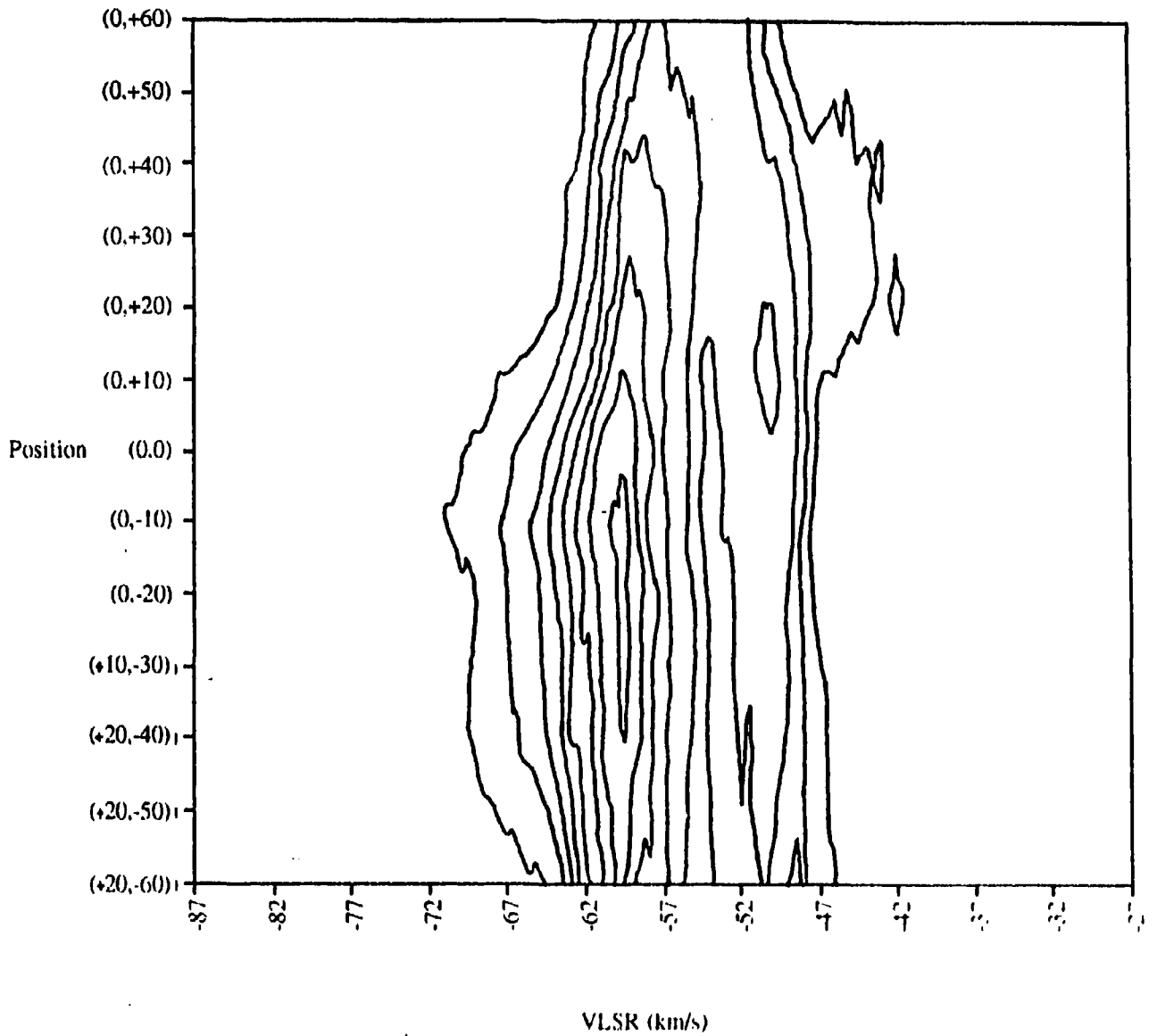


Figure 18. Position-velocity map of CO emission along the major axis of the bipolar molecular outflow associated with NGC 7538 IRS 9. The minimum contour is $10 \text{ K}\cdot\text{km}\cdot\text{s}^{-1}$ with a contour interval of $10 \text{ K}\cdot\text{km}\cdot\text{s}^{-1}$.

much larger than the inclination of the flow to the line of sight, θ . The shape of the blueshifted velocity field indicates that the blue emission lobe remains uniform with changing velocity. We may note that velocity of the outflow is independent of position over a considerable distance which is consistent with a model where the flow velocity remains constant (Cabrit 1990). The radial velocity of the redshifted gas appears to increase with distance from the center of the flow implying acceleration.

Our calculations of the excitation temperature using equation (6) and assuming a beam filling factor of unity show that $T_{\text{ex}} = 20 - 35$ K throughout the uncontaminated inner wings. Kameya *et al.* (1989) use an excitation temperature of 35 K for their calculations. We, therefore, adopt a value of $T_{\text{ex}} = 35$ K with which we may calculate the outflow properties for NGC 7538 IRS 9 as described in §2c. The results are displayed in Tables 4 and 5. Using both methods as described in §2c we calculate the dynamical timescale to obtain outflow ages of $t_1 = 29,800$ years and $t_2 = 65,500$ years. The outflow mass for the blueshifted gas was found to be 47 M_{\odot} while that of the redshifted gas was 2.5 M_{\odot} giving a total outflow mass of 49.5 M_{\odot} . The calculated outflow mass of the blueshifted gas is much larger than that of the redshifted gas which may be due largely to the exclusion of the optically thick region of the red wing in which the unrelated $-49 \text{ km}\cdot\text{s}^{-1}$ cloud is found (ie. $-47 \text{ km}\cdot\text{s}^{-1}$ to $-52 \text{ km}\cdot\text{s}^{-1}$). The total outflow momentum and kinetic energy were calculated to be $\sim 297 M_{\odot} \text{ km/s}$ and 2.3×10^{46} ergs respectively. Dividing kinetic energy by dynamical timescale (t_1 and t_2 separately) we obtain mechanical luminosity, $L_1 = 6.7 L_{\odot}$ and $L_2 = 3.0 L_{\odot}$. The corresponding mass loss rates are $\dot{M}_1 = 1.7 \times 10^{-3} M_{\odot}/\text{yr}$ and $\dot{M}_2 = 7.6 \times 10^{-4} M_{\odot}/\text{yr}$.

TABLE 4
DYNAMICAL TIMESCALES

Source	Distance (kpc)	V_{\max}^a (km/s)	$\langle V \rangle^b$ (km/s)	R_{\max}^c (km)	R_{cen}^d (km)	$t_1 = R_{\max}/V_{\max}$ (yr)	$t_2 = R_{\text{cen}}/\langle V \rangle$ (yr)
GL 490	1.0	37	8.5	1.3×10^{13}	3.8×10^{12}	11,300	10,700
NGC 7538 IRS 9	2.7	34	6	3.2×10^{13}	1.3×10^{13}	29,800	65,500

^a V_{\max} = half the total line width.

^b $\langle V \rangle$ = the total momentum divided by the total mass.

^c R_{\max} = half the total major axis of the flow.

^d R_{cen} = half the distance between the blue and red centroids.

TABLE 5
PHYSICAL PROPERTIES OF THE OUTFLOWS

Source	Mass (M_{\odot})			Momentum		L (L_{\odot})		\dot{M} (M_{\odot}/yr)	
	M_{blue}	M_{red}	M_{tot}	$M_{\odot} \text{ km/s}$	E_{kin} (erg)	L_1	L_2	\dot{M}_1	\dot{M}_2
GL 490	3.9	4.8	8.7	74	8.3×10^{45}	6.8	6.5	8.2×10^{-4}	5.9×10^{-4}
NGC 7538 IRS 9	47	2.5	49.5	297	2.3×10^{46}	6.7	3.0	1.7×10^{-3}	7.6×10^{-4}

IV. DISCUSSION

The observed high-velocity motions of the molecular gas around GL 490 ($V_{\max} = 37 \text{ km}\cdot\text{s}^{-1}$) and NGC 7538 IRS 9 ($V_{\max} = 34 \text{ km}\cdot\text{s}^{-1}$) are due to energetic mass loss in the form of a massive bipolar outflow of cold and clumpy molecular gas from embedded YSOs. The process of vigorous mass ejection from YSOs is, at present, the earliest observationally identifiable stage of stellar evolution. The kinetic energies associated with these outflows are very large ($\sim 10^{46}$ ergs), creating the problem of determining the driving mechanism. Radiation pressure alone cannot power the outflow.

GL 490 and NGC 7538 IRS 9 have been fully mapped in the CO J = 2 \rightarrow 1 transition with an angular resolution of 21". Our observations are the best, to date, for these objects. Our knowledge of the spatial extent of the outflow gas allows us to calculate the momentum and other related properties of the outflow. In the case of GL 490 we may compare our results with those of Snell *et al.* (1984). They find a mass-weighted velocity, $\langle V \rangle$, of $8.6 \text{ km}\cdot\text{s}^{-1}$ compared to our $8.5 \text{ km}\cdot\text{s}^{-1}$. Using method 2 in §2c ($t_2 = R_{\text{cen}}/\langle V \rangle$) for determining the dynamical timescale they find $t_2 = 17,000$ years whereas we find $t_2 = 10,700$ years. Their results for the total outflow mass, momentum, and kinetic energy are $15.4 M_{\odot}$, $133 M_{\odot}\cdot\text{km}\cdot\text{s}^{-1}$, and 1.4×10^{46} ergs respectively compared to our $8.7 M_{\odot}$, $74 M_{\odot}\cdot\text{km}\cdot\text{s}^{-1}$, and 8.3×10^{45} ergs respectively. The results obtained for NGC 7538 IRS 9 cannot readily be compared with any previous work. We find the total outflow mass, momentum, and kinetic energy to be $49.5 M_{\odot}$, $297 M_{\odot}\cdot\text{km}\cdot\text{s}^{-1}$, and 2.3×10^{46} ergs respectively.

Two definitions were used for the dynamical timescale of the outflow (§2c). For GL 490 we find that the two methods yield very similar ages; $t_1 = 11,300$ years and $t_2 = 10,700$ years. The dynamical timescales for NGC 7538 IRS 9 are found to be within a

factor of 2.2 of each other; $t_1 = 29,800$ years and $t_2 = 65,500$ years. The difference in ages of these two objects is relatively small ($\sim 1 \times 10^4$ and $\sim 3 \times 10^4$ yr. for t_1), implying that these objects are close in age. The mass loss rate for both objects is similar regardless of the method used to determine the dynamical timescale ($\sim 0.6 \times 10^{-3}$ and $1.7 \times 10^{-3} \text{ MO}\cdot\text{yr}^{-1}$) indicating that the same mechanism is responsible for the mass loss.

In comparing the mechanical luminosity to the stellar luminosity of the driving source (see Table 6 and Fig. 19) we note that a very small fraction of the sources' luminosity is transported to the molecular cloud, demonstrating that enough energy is available to create the observed mechanical luminosity. The momentum flux of the gas, however, is much greater than that of the source. Figure 20 displays this in a plot of force vs. radiant luminosity of the central source. Also plotted in Figure 20 is the relation $\dot{M}V = L*/c$, where $L*/c$ is the force exerted on the gas if every photon emitted by the central object is absorbed. Since all the sources in Table 6 fall above this relation, radiation pressure alone cannot be the driving mechanism unless thermal re-radiation by dust grains is incorporated. Radiation is multiply absorbed and re-radiated as it traverses the envelope surrounding the protostar. The resulting momentum transfer may exceed that due to the direct stellar component $L*/c$, assuming the surrounding envelope is optically thick (Phillips & Beckman, 1980). Many flow central sources, however, are optically visible which makes the above situation unlikely (Lada 1985).

The "+" and "o" symbols in Figures 19 and 20 represent the values obtained for mechanical luminosity and momentum flux using the different methods described in §2c to calculate dynamical timescale, t_1 and t_2 respectively. Mechanical luminosities for GL 490 were $L_1 = 6.8 \text{ LO}$ and $L_2 = 6.5 \text{ LO}$ and for NGC 7538 IRS 9 were $L_1 = 6.7 \text{ LO}$ and $L_2 = 3.0 \text{ LO}$. Outflow momentum flux for GL 490 were $\dot{M}V_1 = 0.03 \text{ MO}\cdot\text{yr}^{-1}\cdot\text{km}\cdot\text{s}^{-1}$ and $\dot{M}V_2 = 0.02 \text{ MO}\cdot\text{yr}^{-1}\cdot\text{km}\cdot\text{s}^{-1}$ and for NGC 7538 IRS 9 were $\dot{M}V_1 = 0.058 \text{ MO}\cdot\text{yr}^{-1}\cdot\text{km}\cdot\text{s}^{-1}$ and

TABLE 6
PHYSICAL PARAMETERS OF OTHER OUTFLOWS

Source	L_{HMF} (L_{\odot})	$\dot{M}V$ ($M_{\odot} \cdot \text{km} \cdot \text{s}^{-1} \cdot \text{yr}^{-1}$)	L_{*} (L_{\odot})
GL 490	6.8	3.0×10^{-2}	1400 ^c
NGC 7538 IRS 9	6.7	5.8×10^{-2}	40,000 ^d
^a M8E-IR	0.5	1.7×10^{-3}	25,000 ^b
^a GL 2591	2.3	8.2×10^{-3}	20,000 ^e
^a W3 IRS5	3.1	2.4×10^{-2}	700,000 ^e
^b LKH α 198	0.02	4.0×10^{-5}	1000
^b HH 7-11	6.4	4.0×10^{-3}	90
^b L1551-IRS5	0.2	2.0×10^{-4}	25
^b Orion A	2600	5.2×10^{-1}	10,000
^b HH 24	0.24	4.0×10^{-4}	20
^b NGC 2071	175	6.0×10^{-2}	750
^b Mon R2	240	2.0×10^{-2}	50,000
^b AFGL 961	11	7.0×10^{-3}	5500
^b PV Cep	0.03	8.5×10^{-4}	80
^b LKH α 234	1.0	2.0×10^{-3}	1000

^a Mitchell, Hasegawa, & Schella, 1992.

^b excerpt from Table 3 of Lada, 1985.

^c Harvey *et al.*, 1979.

^d Mitchell & Hasegawa, 1991.

^e Mozurkewich, Schwartz, & Smith, 1986.

Table 6. This table lists the flow mechanical luminosity, L_{HMF} , the momentum flux, $\dot{M}V$, and the source stellar luminosity, L_{*} , for various sources (including those studied in this thesis).

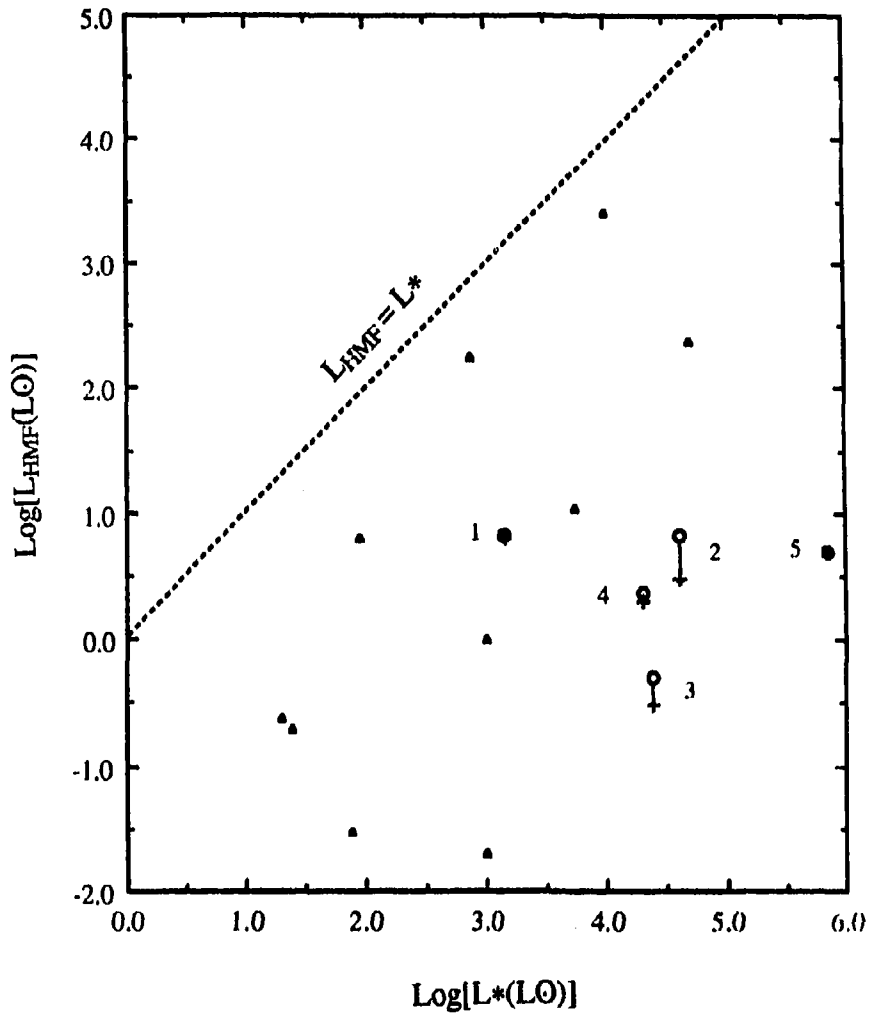


Figure 19. Mechanical luminosity of high-velocity molecular outflows plotted against the total radiant luminosity of embedded central objects. All sources fall below the relation $L_{\text{HMF}} = L^*$. A " \blacktriangle " represents the data from Lada (1985), while " \circ " and " $+$ " represent the data for L_1 and L_2 respectively.

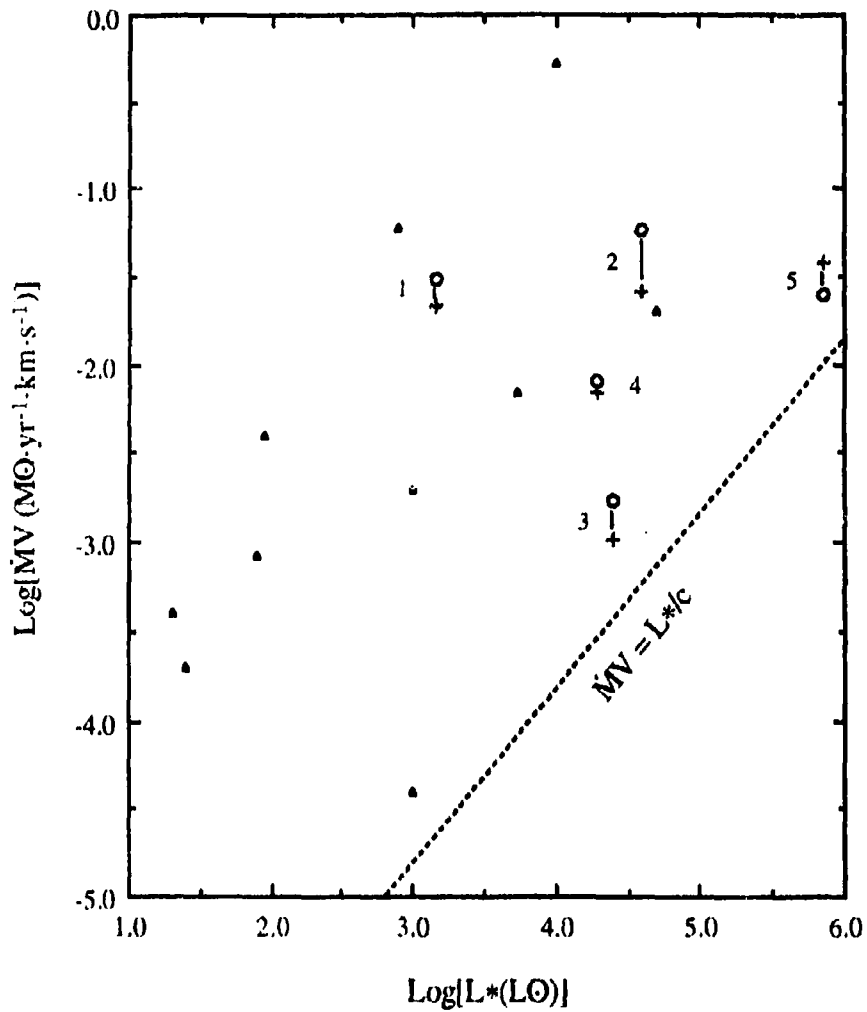


Figure 20. Momentum flux of high-velocity molecular outflows plotted against the total radiant luminosity of embedded central objects. All sources fall above the relation $MV = L*/c$. A "▲" represents the data from Lada (1985), while "○" and "+" represent the data for MV_1 and MV_2 respectively.

$\dot{M}V_2 = 0.026 \text{ M}\odot\cdot\text{yr}^{-1}\cdot\text{km}\cdot\text{s}^{-1}$. The mechanical luminosity and momentum flux for GL 490 and NGC 7538 IRS 9 are quite similar to the other objects listed in Table 6, indicating similar mass loss mechanisms for these sources.

Lada (1985) suggests that a correlation of $\dot{M}V$ and L_{HMF} with L^* may exist and may provide fundamental clues to the nature of the outflows. If such a correlation exists, this suggests that the energetics of an outflow are determined by either the mass or luminosity of the central object, as one might expect if a star is the driving source. The above correlation also suggests that the same mechanism is responsible for all of the outflows.

As was shown in the contour plots of integrated intensity (Figures 10 and 16), both outflows are bipolar. These data show a clear separation of $\sim 70''$ between the red and blueshifted emission lobes in NGC 7538 IRS 9 indicating bipolarity clearly for the first time in this object. A separation of $40''$ is observed between the red and blue emission lobes in GL 490. Despite a slight offset of the midpoint of the line connecting these two peaks we still believe that the IR sources are the driving objects behind the high-velocity outflows. This apparent offset may be due to a number of factors such as pointing error, resolution of the observations, and could possibly be due to some inhomogeneity in the surrounding ambient cloud as well as motion as small as a few km/s of the IR source with respect to the ambient cloud, as suggested by Snell *et al.* (1984).

In the case of NGC 7538 IRS 9, Kameya *et al.* (1989) give a weak argument for the existence of a circumstellar disk surrounding the central source on the basis of the apparent relationship between the blueshifted lobe and a nearby reflection nebula. They have observed in an optical CCD image that the brightness of the reflection nebula decreases toward the source. They suggest that only the near side of the reflection nebula is visible whereas the far side is not, due to heavy extinction by the molecular disk. This heavy

extinction is observed in the infrared by Werner *et al.* (1979) and by Eiroa, Lenzen, and Gomez (1988) who observe a visual extinction of greater than 25.4 magnitudes.

The results of our study can be summarized as follows:

1. Broad CO emission wings were observed. Total line widths (at $T_A^* = 0.2$ K level) were $74 \text{ km}\cdot\text{s}^{-1}$ for GL 490 and $68 \text{ km}\cdot\text{s}^{-1}$ for NGC 7538 IRS 9.
2. Contour maps clearly show bipolarity for both GL 490 and NGC 7538 IRS 9 with separations of $40''$ and $70''$ respectively between the red and blue emission peaks. In the case of NGC 7538 IRS 9, this is the first conclusive evidence of bipolarity available.
3. ^{13}CO observations indicate that the CO emission is optically thick for the inner wing gas. The mean optical thickness is ~ 5 for GL 490 and ~ 8 for NGC 7538 IRS 9.
4. For GL 490 we find the total outflow mass, momentum, and kinetic energy of 8.7 M_\odot , $74 \text{ M}_\odot\cdot\text{km}\cdot\text{s}^{-1}$, and 8.3×10^{45} ergs respectively. The dynamical timescales for GL 490 were $t_1 = 11,300$ years and $t_2 = 10,700$ years. We find the total outflow mass, momentum, and kinetic energy for NGC 7538 IRS 9 to be 49.5 M_\odot , $297 \text{ M}_\odot\cdot\text{km}\cdot\text{s}^{-1}$, and 2.3×10^{46} ergs respectively. The dynamical timescales for NGC 7538 IRS 9 were $t_1 = 29,800$ years and $t_2 = 65,500$ years.
5. The results of this paper have shown large masses and moderate velocities of the observed molecular gas, implying that we are seeing the swept-up ambient gas rather than the original ejected material.
6. The excitation temperatures used ($T_{\text{ex}} = 20$ K for GL 490 and $T_{\text{ex}} = 35$ K for NGC 7538 IRS 9) are similar to the temperatures of the ambient cloud, implying that the emission arises from gas far behind the shock front where the gas has already cooled.
7. A position-velocity map (Fig. 12) indicates that the GL 490 outflow is decelerating. Figure 11, however, shows acceleration of the gas at velocities greater than $12 \text{ km}\cdot\text{s}^{-1}$. These figures do not contradict each other, however, since the position-velocity map does not cover the region where the accelerated gas is prominent. The overlapping blue and red

emission lobes indicates that the flow opening angle, θ_{max} , is greater than the inclination angle, θ , of the flow to the line of sight (ie. $\theta_{\text{max}} > \theta$). Some evidence for shell structure can also be seen in Figure 12.

8. In NGC 7538 IRS 9 the position-velocity map (Fig. 18) is consistent with constant flow velocity for the blueshifted gas and infers acceleration for the redshifted gas with velocities greater than $-47 \text{ km}\cdot\text{s}^{-1}$. The red and blue emission lobes do not overlap by very much, implying that θ_{max} is only slightly greater than θ . No evidence for shell structure can be seen.

9. The physical parameters calculated for GL 490 and NGC 7538 IRS 9 are found to be comparable to other luminous sources. Figures 19 and 20 show that a correlation exists between L_{HMF} and L^* , as well as between $\dot{M}V$ and L^* . A correlation such as this indicates that the same mechanism is responsible for all outflows.

10. The observations presented here do not favor a particular outflow model, although the Pudritz and Norman model of centrifugally driven disk winds could be applicable. The sources studied in this thesis are deeply embedded in molecular clouds, indicating that massive accretion disks are to be expected. No evidence, however, of the predicted rotation of the outflowing gas has been found.

REFERENCES

- Arquilla, R. and Goldsmith, P.F. 1986, *Ap.J.*, **303**, 356.
- Bally, J. and Lada, C.J. 1983, *Ap.J.*, **265**, 824.
- Bowers, R. and Deeming, T. 1984, *Astrophysics I*, Boston: Science Press.
- Cabrit, S. 1991, preprint.
- Cabrit, S. and Bertout, C. 1990, *Ap.J.*, **348**, 530.
- . 1986, *Ap.J.*, **307**, 313.
- Campbell, B., Persson, S.E. 1988, *A.J.*, **95**, 1185.
- Campbell, B., Persson, S.E., and McGregor, P.J. 1986, *Ap.J.*, **305**, 336.
- DeCampli, W. 1981, *Ap.J.*, **224**, 124.
- Dickman, R.L. 1978, *Ap.J. Suppl.*, **37**, 407.
- Eiroa, C., Lenzen, R., and Gomez, A.I. 1988, *Astr.Ap.*, **190**, 283.
- Erickson, N.R., Goldsmith, P.F., Snell, R.I., Berson, R.L., Huguenin, G.R., *et al.*
1982, *Ap.J. Lett.*, **261**, L103.
- Fischer, J., Righini-Cohen, G., Simon, M., Joyce, R.R., and Simon, T. 1980, *Ap.J. Lett.*, **240**, L95.
- Genzel, R., Reid, M.J., Moran, J.M., and Downes, D. 1981, *Ap.J.*, **224**, 884.
- Goldsmith, P.F., Snell, R.L., Hemeon-Heyer, M., and Langer, W.P. 1984, *Ap.J.*, **286**, 599.
- Harvey, P.M., Campbell, M.F., Hoffmann, W.F., Thronson, H.A., and Gatley, I.
1979, *Ap.J.*, **229**, 990.
- Herbig, G.H. 1977, *Ap.J.*, **217**, 693.
- Herbig, G.H. and Jones, B.F. 1981, *Astron. J.*, **86**, 1232.
- . 1981, *Astron. J.*, **88**, 1040.
- Hodapp, K.-W. 1990, *Ap.J.*, **352**, 184.
- Hodapp, K.-W. 1984, *Astr.Ap.*, **141**, 255.

- Jaffe, D.T., Güsten, R., and Downes, D. 1981, *Ap.J.*, **250**, 621.
- Kaifu, N., Suzuki, S., Hasegawa, T., and Oishi, M. 1985, *Nobeyama Radio Obs. Graphic Rep No.15*.
- Kameya, O., Hasegawa, T.I., Hirano, N., and Takakubo, K. 1989, *Ap.J.*, **339**, 222.
- Kawabe, R., Ogawa, H., Fukui, Y., Takano, T., Fujimoto, Y., Sugitani, K., and Fujimoto, M. 1984, *Ap.J. Lett.*, **282**, L73.
- Koo, B.-C. 1989, *Ap.J.*, **337**, 318.
- Lada, C.J. 1985, *Ann.Rev.Astron.Astrophys.*, **23**, 267.
- Lada, C.J. and Harvey, P.M. 1981, *Ap.J.*, **245**, 58.
- Lizano, S., Heiles, C., Rodriguez, L.F., Koo, B.-C., Shu, F.H., Hasegawa, T., Hayashi, S., and Mirabel, I.F. 1988, *Ap.J.*, **328**, 763.
- Margulis, M. and Lada, C.J. 1985, *Ap.J.*, **299**, 925.
- Merrill, K.M., Russell, R.W., and Soifer, B.T. 1976, *Ap.J.*, **207**, 763.
- Minchin, N.R., Hough, J.H., Burton, M.G., and Yamashita, T. 1991, *Mon.Not.R.Ast.Soc.*, **251**, 522.
- Mitchell, G.F., Hasegawa, T.I., Schella, J. 1992, *Ap.J.*, in press.
- Mitchell, G.F. and Hasegawa, T.I. 1991, *Ap.J. Lett.*, **371**, L33.
- Mitchell, G.F., Maillard, J.-P., and Hasegawa, T.I. 1991, *Ap.J.*, **371**, 342.
- Mitchell, G.F., Curry, C., Maillard, J.-P., and Allen, M. 1989, *Ap.J.*, **341**, 1020.
- Morris, M., Palmer, P., Turner, B.E., and Zuckerman, B. 1974, *Ap.J.*, **191**, 349.
- Mozurkewich, D., Schwartz, P.R., and Smith, H.A. 1986, *Ap.J.*, **311**, 371.
- Mundy, L.G. and Adelman, G.A. 1988, *Ap.J.*, **329**, 907.
- Padman, R. 1988, *SPECX V5.3 Users' Manual*, Cambridge: Cavendish Laboratory.
- Persson, S.E., Geballe, T.P., McGregor, P.J., Edwards, S., and Lonsdale, C.J. 1984, *Ap.J.*, **286**, 289.
- Phillips, J.P., White, G.J., Rainey, R., Avery, L.W., Richardson, K.J., Griffin, M.J., *et al.* 1988, *Astr.Ap.*, **190**, 289.

- Phillips, J.P. and Beckman, J.E. 1980, *Mon.Not.R.Ast.Soc.*, **193**, 245.
- Pudritz, R.E. 1985, *Ap.J.*, **293**, 216.
- Pudritz, R.E. and Norman, C.A. 1983, *Ap.J.*, **274**, 677.
- . 1986, *Ap.J.*, **301**, 571.
- Reipurth, B. 1990, *IAU Symposium 137, Flare Stars in Star Clusters, Associations, and the Solar Vicinity*, preprint.
- Scoville, N.Z., Sargent, A.I., Sanders, D.B., Claussen, M.J., Masson, C.R., Lo, K.Y., and Phillips, T.G. 1986, *Ap.J.*, **303**, 416.
- Shu, F.H., Adams, F.C., and Lizano, S. 1987, *Ann.Rev.Astron.Astrophys.*, **25**, 23.
- Shull, J.M. and Beckwith, S. 1982, *Ann.Rev.Astron.Astrophys.*, **20**, 163.
- Simon, M., Felli, M., Cassar, L., Fischer, J., and Massi, M. 1983, *Ap.J.*, **266**, 623.
- Smith, P.A., Brand, P.W.J.L., Mountain, C.M., Puxley, P.J., and Nakai, N. 1991, *Mon.Not.R.Ast.Soc. Short Communication*, **252**, 6P.
- Smith, L.F., Biermann, P., and Mezger, P.G. 1978, *Astr.Ap.*, **66**, 65.
- Snell, R.L., Scoville, N.Z., Sanders, D.B., and Erickson, N.R. 1984, *Ap.J.*, **284**, 176.
- Solomon, P.M., Sanders, D.B., and Rivolo, A.R. 1985, *Ap.J. Lett.*, **292**, L19.
- Spitzer, L.Jr. 1978, *Physical Processes in the Interstellar Medium*, New York: Wiley-InterScience.
- Strom, S.E., Grasdalen, G.L., and Strom, K.M. 1974, *Ap.J.*, **191**, 111.
- Thompson, R.I. and Tokunaga, A.T. 1979, *Ap.J.*, **231**, 736.
- Tokunaga, A.T., Lebofsky, M.J., and Rieke, G.H. 1981, *Astr.Ap.*, **99**, 108.
- Werner, M.W., Becklin, E.E., Gatley, I., Matthews, K., and Neugebauer, G. 1979, *Mon.Not.R.Ast.Soc.*, **188**, 463.
- Wolf, G.A., Lada, C.J., and Bally, J. 1990, *Astron.J.*, **100**, 1892.

APPENDIX A

The reduction of the initial CO $J = 2 \rightarrow 1$ data requires the use of three programs written for this purpose: (1) SPECX (Padman, 1988), (2) PROFILE.FOR, and (3) COLDEN.FOR. These programs can be found in the Saint Mary's VAX account SPECX. The program SPECX allows one to examine the raw CO profile data (which has been converted from observed intensity to antenna temperature) and to determine such things as the integrated intensity for a given velocity range as well as creating contour plots and channel maps. This approach to calculating outflow mass and other related physical properties, however, was found to be cumbersome and time consuming. In order to facilitate the data reduction process we use two other programs written expressly for this purpose. What follows is a step-by-step explanation of how to use these three programs for the data reduction. All commands to be entered by the user will be denoted by {} around the command.

In order to manipulate the raw CO profile data one must have access to the Saint Mary's VAX account SPECX. Upon entering the account type {SHOW TERMINAL} at the prompt. This gives us the terminal number (LTA____). At the next prompt type {ASSIGN_HUSKY1\$(terminal #)_TXA6}. This assigns the terminal to the device TXA6. One may now enter the directory which contains the spectral data. In our case we simply type {ENTER MP119}. The spectral data in this directory may only be accessed through the program SPECX so, in order to use the program SPECX, type {SPECX}. We now have access to the raw spectral data. We require, however, the two programs PROFILE.FOR and COLDEN.FOR in order to convert the raw data (which is in the form T_A^* vs. bin #) into column densities and finally into mass, momentum, and kinetic energy.

This requires that we copy the raw data into a file which is accessible to these two programs. This method is explained below.

Before entering SPECX we must first initiate the VAX command called PHOTO. To begin we must type {SETUP_PHOTO}. After this is done we type {PHOTO} and everything entered proceeding this will be placed into a file called PHOTO.LOG. Once PHOTO has been initiated we must then enter SPECX. If the desired file is not open we type {OPEN-FILE} and then enter the file name. To open the desired profile type {READ-DATA} and the computer will prompt for a scan number. Enter the appropriate scan number, then type {PRINT-SPECTRUM-HEADER}, which lists the frequency and temperature information. Next type {LIST-SPECTRUM}. This lists the raw profile data, T_A^* vs. bin #. At the next prompt type {EXIT} to leave SPECX. This puts you back in the directory MP119. We then end the photo sequence by typing {LOGOUT}. You now have all the data for one profile copied into the file PHOTO.LOG.

The next step is to move this data file to the REDUCE directory where the data reduction programs are stored. At the prompt type {ENTER_REDUCE}. In order to copy a file from the directory where the original data is stored (in this case MP119) to directory REDUCE, we type {COPY_[JCMTUSER.OBSERVE.MP119]PHOTO.LOG_filename}. The filename must end in {.DAT}. Follow this procedure for however many spectra you wish to copy. After this has been done we may now implement the FORTRAN programs PROFILE.FOR and COLDEN.FOR.

The purpose of PROFILE.FOR is to convert the SPECX data file into integrated intensity, momentum, and kinetic energy data for a selected velocity range. If one already has data for a ^{13}CO profile and the data for the corresponding ^{12}CO profile a line ratio may be taken to determine the optical depth for each channel.

In order to calculate the integrated intensity, momentum, and kinetic energy for the CO gas, one must first use PROFILE.FOR to determine the appropriate bin numbers for the desired velocity ranges as well as the bin number corresponding to the main peak. Once the bin numbers have been obtained we may begin by typing (RUN PROFILE). The following is a numbered sequence of steps to follow once in PROFILE.FOR:

- (1) Enter the frequency interval which corresponds to the channel width.
- (2) Do you wish to create a new file? To calculate the energetics enter {Y} and go to step (3) below, otherwise, enter {N} to calculate a line ratio and go to step (9).
- (3) Enter the original filename.
- (4) Enter the name of the file you wish to store the bin #, T_A^* , and $V_{I,SR}$ data in.
- (5) Enter the name of the file in which the integrated intensity, momentum, and kinetic energy data will be stored.
- (6) Enter the channel range corresponding to the desired velocity range.
- (6a) Enter the bin number corresponding to the main peak. This number is entered only once for each profile.
- (7) Do you wish to view the temperature and velocity output?: {Y} or {N}. This is your option, though it will be useful in determining if the correct channel range is being used. If you then want to calculate the energetics type {Y}.
- (8) Do you wish to read from the same file?: {Y} or {N}. If the same file is used go back to step (6) and follow the same procedure as outlined (except step 6a). This allows one to store all of the energetics data for various velocity ranges into the same file. If another file (ie. a different profile) is used go back to step (3) and follow the same procedure.
- (9) Do you want to compute a line ratio?: {Y} or {N}. If {Y} continue with step (10). If {N} you have ended the program.
- (10) Enter the file name for the ^{12}CO profile.

- (11) Enter the file name for the ^{13}CO profile.
- (12) Input the abundance ratio, R. $R = 89$ for a solar abundance ratio.

After step (12), the program displays the velocity, the ratio T_A^{13}/T_A^{12} , T_{ex} , τ^{12} , and τ^{13} for each bin. After this is done the program then displays the velocity, ^{13}CO column density for $J = 0$ rotational level, ^{13}CO column density for $J = 1$ rotational level, and the total ^{13}CO column density for each bin.

COLDEN.FOR calculates the total mass, momentum, and kinetic energy for each velocity range as well as for the entire profile. What follows are the steps required in using the program. Begin by typing **{RUN COLDEN.FOR}** then start at step (1):

- (1) Enter the file name which contains the integrated intensity, momentum, and kinetic energy data for the CO gas. This is the file produced by **PROFILE.FOR**.
- (2) Enter the value for T_{ex} .
- (3) Do you wish $\tau^{12} < 1$ for the inner wing? **{Y}** or **{N}**. If **{Y}**, you assume optically thin wings. If **{N}**, you assume the inner wing is optically thick, in which case you must enter the program previous to running it and set the optical depth for the velocity intervals relating to the thick part of the wing.

The program then outputs to the screen. First, the ^{12}CO column density (N_{CO}), $(v-v_0)N_{\text{CO}}$, and $(v-v_0)^2N_{\text{CO}}$ for each velocity range are displayed. Secondly, the mass, M_{H_2} , the momentum, $(v-v_0)M_{\text{H}_2}$, and the kinetic energy, $(v-v_0)^2M_{\text{H}_2}$, for each velocity range are displayed. Finally, the above quantities are summed up over the entire profile and totals for the blue wing, red wing, and total profile are displayed.

APPENDIX B

PROFILE.FOR

```
PARAMETER (K = 2050, KK = 65000)
REAL I, QUAD, CENTCH, RESTFR, OBSFR, INCFR, TSYS, FREQIN
REAL DELV, VBIN1(K), BIN1(K), VEL1(K), TEMP1(K), TEMPTOT
REAL SBIN(K), LBIN(K), STEMP(K), LTEMP(K), SVBIN(K), LVBIN(K)
REAL D12, D13, CVEL, DVEL, SUM3, SUM4, TEMP12(K), TEMP13(K)
REAL RF12, RF13, V0, DV, MOM, T13(KK), TAU13(K), X1, SUM, ADD
REAL TR12(K), TR13(K), TEX(K), X2, SUMTAU, N13J0(K), N13J1(K)
REAL N13J1A, N13CO(K), Q13(K), NSUM, INT, TAU12(K), KE, DKE
REAL TRMS, DINT, DMOM, TYN
INTEGER BINV0, L, N, L12, L13, N12, N13, TPEAK, NTON, NBIN, FI
CHARACTER*8 FILNAM, FILNAM12, FILNAM13, START, YN, DUMMY
CHARACTER*12 DATNAM, DATANAM
CHARACTER*16 SPECTIT
CHARACTER*72 SCAN

C = 2.9979*1E5
ETAB12 = 0.71
ETAB13 = 0.71
TYPE *, ' ENTER THE FREQUENCY INTERVAL'
ACCEPT 5, INCFR
5  FORMAT (F8.5)
   FI = 999
TYPE *, ' DO YOU WISH TO CREATE ANY NEW FILES (Y/N)?'
ACCEPT 10, YN
IF (YN .EQ. 'N') GOTO 100
1  TYPE *, ' ENTER THE ORIGINAL FILE NAME'
   ACCEPT 10, FILNAM
10  FORMAT (1A8)
   TYN = 0.0
   ADD = 0.0

OPEN (UNIT = 1, FILE = FILNAM, TYPE = 'OLD', READONLY)
C
C  GET PARAMETERS ** REST FREQ., OBS. FREQ., INCREMENT FREQ. **
C
DO 13 I = 1, K
  READ (1,10) START
  IF (START .EQ. '-----') GOTO 14
13  CONTINUE

14  READ (1,10) DUMMY
   READ (1,9) SCAN
9   FORMAT (A72)

DO 15 I = 1, K
  READ (1,10) START
```

```

15     IF (START .EQ. 'Quad. #') GO TO 17
      CONTINUE

C     *****
C     *** CALCULATE THE VELOCITY INCREMENT ***
C     *****

17     READ (1,*) QUAD, N, CENTCH, RESTFR, OBSFR, FREQIN, TSYS
      RESTFR = RESTFR*1E9
      OBSFR = OBSFR*1E9
      IF (FI .EQ. 999) INCFR = INCFR*1E6
      DELV = C*INCFR/RESTFR
      BINV0 = CENTCH - (OBSFR - RESTFR)/INCFR
      VBIN1(1) = (BINV0 - 1)*DELV

C
      DO 20 I = 1, N
        READ (1,10) START
        IF (START .EQ. 'Quadrant') GO TO 30
20     CONTINUE

30     DO 40 I = 1, N, 8
        READ (1,*) BIN1(I), (TEMP1(J), J = 1, I+7)
        DO 35 L = I, I+7
          BIN1(L+1) = BIN1(L) + 1
          VBIN1(L+1) = VBIN1(L) - DELV
35     CONTINUE
40     CONTINUE

C     *****
C     ** PRINTOUT OF DESIRED RANGE **
C     *****

      WRITE (*,*) ' '
      TYPE *, ' ENTER THE FILE NAME TO WHICH THE TEMPERATURE DATA
WILL BE STORED'
      ACCEPT 43, DATNAM
43     FORMAT (1A12)
      WRITE (*,*) ' '
      WRITE (*,*) ' VELOCITY EQUALS ZERO AT CHANNEL #',BINV0
      WRITE (*,*) ' '
      WRITE (*,*) ' VELOCITY INCREMENT IS',DELV
      WRITE (*,*) ' '

      TYPE *, ' ENTER THE FILE NAME TO WHICH ENERGETICS ARE
STORED'
      ACCEPT 43, DATANAM
      OPEN (UNIT = 6, FILE = DATANAM, STATUS = 'NEW')

44     INT = 0.0
      MOM = 0.0
      KE = 0.0
      TYPE *, ' ENTER THE DESIRED CHANNEL RANGE (0,0 FOR WHOLE
RANGE):'
      ACCEPT 45, L, N

```

```

45  FORMAT (I5,I5)
    IF (L .EQ. 0 .AND. N .EQ. 0) THEN
        L = 1
        N = 2050
    ENDIF
C
    IF (ADD .EQ. 1.0) GOTO 48
    TYPE *, ' ENTER BIN NUMBER FOR MAIN PEAK'
    ACCEPT 53, TPEAK
53  FORMAT (I6)
    V0 = VBIN1(TPEAK)
    ADD = 1.0
C
48  TYPE *, ' DO YOU WISH TO VIEW THE OUTPUT (Y OR N)'
    ACCEPT 47, Y
47  FORMAT (A2)
    IF (Y .EQ. 'N') GO TO 55
    WRITE (*,*) ' '
    WRITE (*,*) ' BIN #    TEMP    VELOCITY'
    DO 50 I = L, N
        WRITE (*,801) BIN1(I), TEMP1(I), VBIN1(I)
50  CONTINUE

55  OPEN (UNIT = 2, FILE = DATNAM, STATUS = 'NEW')
    WRITE (2,802) DELV, RESTFR, L, N, V0
    WRITE (2,*) ' C'
    WRITE (2,*) ' BIN #    TEMP    VELOCITY'
    WRITE (2,*) ' '
    DO 60 I = L, N
        WRITE (2,801) BIN1(I), TEMP1(I), VBIN1(I)
60  CONTINUE
    CLOSE (UNIT = 1)
    CLOSE (UNIT = 2)
C
    TYPE *, ' DO YOU WANT TO CALCULATE THE ENERGETICS? Y/N'
    ACCEPT 10, Y
    IF (Y .EQ. 'N') GOTO 70
    OPEN (UNIT = 3, FILE = DATNAM, STATUS = 'OLD', READONLY)
    DO 600 I = 1, K
        READ (3,10) START
        IF (START .EQ. ' ') GOTO 610
600  CONTINUE
610  NBIN = N - L + 1
    WRITE(*,*) ' '
    IF (TYN .EQ. 1.) GOTO 606
    TYPE *, ' ENTER T(RMS)'
    ACCEPT 605, TRMS
605  FORMAT (F8.3)
    WRITE (6,*) SCAN
    WRITE (6,811) TRMS
    WRITE (6,*) ' '
    WRITE (6,*) 'VELOCITY RANGE    INTEGRATED INT.    MOMENTUM
*      KINETIC ENERGY'

```

```

606  DINT = ABS(DELV)*NBIN**.5*TRMS
      DO 620 I = L, N
          READ (3,801) BIN1(I), TEMP1(I), VBIN1(I)
          DV = VBIN1(I) - V0
          MOM = DV*TEMP1(I)*ABS(DELV) + MOM
          INT = TEMP1(I)*ABS(DELV) + INT
          KE = DV**2*TEMP1(I)*ABS(DELV) + KE
620  CONTINUE
      DMOM = ((VBIN1(L) + VBIN1(N))/2 - V0)*DINT
      DKE = ((VBIN1(L) - V0)**2 + (VBIN1(L) - V0)*(VBIN1(N) - V0) +
*      (VBIN1(N) - V0)**2)/3*DINT
      WRITE (*,*) ' THE INTEGRATED INTENSITY IS', INT,'+', DINT
      WRITE (*,*) ' '
      WRITE (*,*) ' THE TOTAL MOMENTUM IS', MOM,'+', DMOM
      WRITE (*,*) ' '
      WRITE (*,*) ' THE TOTAL KINETIC ENERGY IS', KE,'+', DKE
      WRITE(6,810) VBIN1(L), VBIN1(N), INT, DINT, MOM, DMOM, KE, DKE

70   TYPE *, ' ARE YOU READING FROM THE SAME FILE? Y/N'
      ACCEPT 10, YN
      IF (YN .EQ. 'N') THEN
          WRITE (*,*) ' '
          TYPE *, ' ARE YOU READING ANOTHER FILE? Y/N'
          ACCEPT 10, YN
          IF (YN .EQ. 'Y') THEN
              FI = 1
              GOTO 1
          ELSE
              GOTO 100
          ENDIF
      ELSE
          TYN = 1.0
          GOTO 44
      ENDIF

C     *****
C     *** RATIO OF 12CO PROFILE TO 13CO PROFILE ***
C     *****

100  CLOSE (UNIT = 3)
      TYPE *, ' DO YOU WANT TO COMPUTE THE LINE RATIO? Y/N'
      ACCEPT 10, YN
      IF (YN .EQ. 'N') THEN
          STOP
      ENDIF
      TYPE *, 'ENTER FILE NAME FOR 12CO PROFILE'
      ACCEPT 10, FILNAM12
      TYPE *, 'ENTER FILE NAME FOR 13CO PROFILE'
      ACCEPT 10, FILNAM13

      OPEN (UNIT = 3, FILE = FILNAM12, TYPE = 'OLD', READONLY)
      OPEN (UNIT = 4, FILE = FILNAM13, TYPE = 'OLD', READONLY)

      READ (3,804) D12, RF12, L12, N12, V0

```

READ (4,804) D13, RF13, L13, N13, V0

IF (ABS(D12) .LT. ABS(D13)) THEN

DELV = ABS(0.5*D13)

GOTO 500

ELSE

DELV = ABS(.5*D12)

GOTO 550

ENDIF

C *****

```
500 DO 510 I = 1, K
      READ (3,10) START
      IF (START .EQ. ' ') GO TO 520
510 CONTINUE
520 DO 525 I = L12, N12
      READ (3,801) SBIN(I), STEMP(I), SVBIN(I)
      TEMP12(I) = STEMP(I)
525 CONTINUE

      DO 530 I = 1, K
        READ (4,10) START
        IF (START .EQ. ' ') GO TO 540
530 CONTINUE
540 DO 545 I = L13, N13
        READ (4,801) LBIN(I), LTEMP(I), LVBIN(I)
        TEMP13(I) = LTEMP(I)
545 CONTINUE

      L = L13
      N = N13
      LN = L12
      NL = N12
      GOTO 200
```

C *****

```
550 DO 560 I = 1, K
      READ (3,10) START
      IF (START .EQ. ' ') GOTO 570
560 CONTINUE
570 DO 575 I = L12, N12
      READ (3,801) LBIN(I), LTEMP(I), LVBIN(I)
      TEMP12(I) = LTEMP(I)
575 CONTINUE

      DO 580 I = 1, K
        READ (4,10) START
        IF (START .EQ. ' ') GOTO 590
580 CONTINUE
590 DO 595 I = L13, N13
        READ (4,801) SBIN(I), STEMP(I), SVBIN(I)
        TEMP13(I) = STEMP(I)
```

595 CONTINUE

L = L12
N = N12
LN = L13
NL = N13

C *****

200 TYPE *, ' INPUT THE VALUE FOR R [R = N(12CO)/N(13CO)]'
ACCEPT 205, NTON

205 FORMAT (I6)

* WRITE (*,*) ' VELOCITY RATIO TEX TAU12
TAU13'

DO 210 I = L, N

CVEL = LVBIN(I) + DELV

DVEL = LVBIN(I) - DELV

DO 220 J = LN, NL

SUM3 = ABS(SVBIN(J) - CVEL)

SUM4 = ABS(SVBIN(J) - DVEL)

IF (SVBIN(J) .LT. CVEL .AND. SVBIN(J) .GT. DVEL) THEN

GOTO 201

ELSE

GOTO 220

ENDIF

C *****

C **** OUTPUT OF TEMPERATURE DATA ****

C *****

201 T13(1) = 0.1

NN = 1

ADD = 0.001

IF (ABS(D12) .LT. ABS(D13)) THEN

TR12(I) = STEMP(J)/ETAB12

TR13(I) = LTEMP(I)/ETAB13

ELSE

TR12(I) = LTEMP(I)/ETAB12

TR13(I) = STEMP(J)/ETAB13

ENDIF

TEMPTOT = ABS(TR13(I)/TR12(I))

IF (TR13(I) .LT. 0.0 .OR. TR12(I) .LT. 0.0) THEN

TEMPTOT = -99.99

TAU13(I) = -99.99

GOTO 208

ENDIF

IF (TEMPTOT .LT. 0.095) ADD = -0.001

DO 206 M = 1, 65000, NN

X1 = (1-EXP(-T13(M)))/(1-EXP(-NTON*T13(M)))

SUM = ABS(TEMPTOT - X1)

IF (SUM .LT. 0.001) THEN

TAU13(I) = T13(M)

GOTO 207

```

                ENDIF
                T13(M+1) = T13(M) + ADD
206      CONTINUE
207      IF (TAU13(I) .LT. 1.0E-4) THEN
                TAU13(I) = 99.99
                GOTO 208
            ENDIF
            TAU12(I) = TAU13(I)*NTON
            X2 = TR13(I)/(10.578*(1-EXP(-TAU13(I)))) + 0.0202887
            TEX(I) = 10.578/LOG(1 + 1/X2)
208      WRITE (*,803) LVBIN(I), TEMPTOT, TEX(I), TAU12(I), TAU13(I)
            IF (TAU13(I) .EQ. -99.99 .OR. TAU13(I) .EQ. 99.99) GOTO 220
            SUMTAU = SUMTAU + TAU13(I)*ABS(D13)

C          *****

220      CONTINUE
210      CONTINUE

            WRITE (*,*) ' '
            WRITE (*,*) ' /T13 dV =', SUMTAU
            WRITE (*,*) ' '

C          *****
C          *** CALCULATIONS OF COLUMN DENSITIES ***
C          *****

            WRITE (*,*) ' '
            WRITE (*,*) ' VELOCITY  N13(J=0)  N13(J=1)  N(13CO)'
            NSUM = 0.0
            DO 230 I = L13, N13
                IF (TEX(I) .EQ. 0.0) THEN
                    N13J1(I) = 99.
                    N13J0(I) = 99.
                    N13CO(I) = 99.
                    GOTO 229
                ENDIF
                N13J1A = 1.5653E-15*(1-EXP(-10.578/TEX(I)))
                N13J1(I) = TAU13(I)*1.5*ABS(D13)/N13J1A
                Q13(I) = 2*TEX(I)/5.289
                N13J0(I) = N13J1(I)/3*EXP(5.289/TEX(I))
                N13CO(I) = Q13(I)*N13J0(I)
                NSUM = NSUM + N13CO(I)
229      WRITE (*,805) LVBIN(I), N13J0(I), N13J1(I), N13CO(I)
230      CONTINUE
            WRITE (*,*) ' '
            WRITE (*,*) ' THE TOTAL COLUMN DENSITY N(13CO) =', NSUM

800      FORMAT (F5.1)
801      FORMAT (2X,F6.1,8X,F6.3,7X,F8.3)
802      FORMAT (F8.3,2X,E12.6,4X,I6,4X,I6,4X,F8.3)
803      FORMAT (F10.3,5X,F8.3,3X,F10.3,4X,F8.3,4X,F8.3)
804      FORMAT (2X,F6.3,2X,F12.6,4X,I6,4X,I6,4X,F8.3)
805      FORMAT (2X,F8.3,4X,E9.3,4X,E9.3,4X,E9.3)

```

```
810  FORMAT (F7.1,F8.1,F11.3,F8.3,F12.3,F9.3,F13.3,F11.3)
811  FORMAT (2X,'T(RMS) =',F6.3)
```

```
STOP
END
```

COLDEN.FOR

```
PARAMETER (K = 15)
REAL VEL1(K), VEL2(K), INT(K), DINT(K), MOM(K), DMOM(K), KE(K)
REAL DKE(K), TEX, NTOT(K), TAU12, SIGMA, CENTVEL, NH2
REAL MTOT(K), KTOT(K), MASS(K), VMASS(K), V2MASS(K)
REAL MH2, KH2, H2, AREA, SUN, MT, VMT, V2MT, DMT, DVMT, DV2MT
REAL INTERR, MOMERR, KEERR, DM(K), DVM(K), DV2M(K), EINT(K)
REAL EMOM(K), EKE(K), NBLUE, MBLUE, KBLUE, NRED, MRED, KRED
REAL BLUM, BLUVM, BLUV2M, REDM, REDVM, REDV2M
CHARACTER*8 FILNAM, START, YN
CHARACTER*72 SCAN
```

```
II = 13
H2 = 2*1.67E-27
AREA = 2.992267E17**2/4
SUN = 1.989E30
```

```
TYPE *, ' ENTER THE FILE NAME'
ACCEPT 5, FILNAM
5  FORMAT (1A8)

OPEN (UNIT = 1, FILE = FILNAM, TYPE = 'OLD', READONLY)
READ (1,10) SCAN
10  FORMAT (A72)
DO 15, I = 1, K
    READ (1,5) START
    IF (START .EQ. ' VELOCIT') GOTO 20
15  CONTINUE

20  WRITE (*,*) ''
    TYPE *, ' ENTER THE VALUE FOR T(EX)'
    ACCEPT 25, TEX
25  FORMAT (F8.3)

TYPE *, 'DO YOU WANT (TAU < 1) FOR THICK WING? (Y/N)'
ACCEPT 26, YN
26  FORMAT (A8)

WRITE (*,*) ''
WRITE (*,*) SCAN
WRITE (*,820) TEX
WRITE (*,*) ''
```

```

DO 30 I = 1, II
  READ (1,800) VEL1(I), VEL2(I), INT(I), DINT(I), MOM(I),
*    DMOM(I), KE(I), DKE(I)
  NTOT(I) = 1.0457E13*TEX*EXP(16.597/TEX)*INT(I)
  MTOT(I) = 1.0457E13*TEX*EXP(16.597/TEX)*MOM(I)
  KTOT(I) = 1.0457E13*TEX*EXP(16.597/TEX)*KE(I)
  SIGMA = ABS(INT(I)/DINT(I))
  CENTVEL = (VEL1(I) + VEL2(I))/2
  IF (YN .EQ. 'Y') GOTO 27
  IF (CENTVEL .GT. 5.0 .OR. CENTVEL .LT. -22.0) GOTO 27
  IF (CENTVEL .LT. 5.0 .AND. CENTVEL .GT. -3.0) TAU12 = 4.0
  IF (CENTVEL .LT. -3.0 .AND. CENTVEL .GT. -7.5) TAU12 = 6.2
  IF (CENTVEL .LT. -7.5 .AND. CENTVEL .GT. -13.5) TAU12 = 24.3
  IF (CENTVEL .LT. -13.5 .AND. CENTVEL .GT. -16.5) TAU12 = 26.4
  IF (CENTVEL .LT. -16.5 .AND. CENTVEL .GT. -18.5) TAU12 = 6.8
  IF (CENTVEL .LT. -18.5 .AND. CENTVEL .GT. -22.0) TAU12 = 3.7
  NTOT(I) = NTOT(I)*TAU12/(1 - EXP(-TAU12))
  MTOT(I) = MTOT(I)*TAU12/(1 - EXP(-TAU12))
  KTOT(I) = KTOT(I)*TAU12/(1 - EXP(-TAU12))
27  IF (CENTVEL .LT. -18.5 .AND. CENTVEL .GT. -22.0) THEN
    IF (INT(I) .GT. 1.83*INT(I-1)) GOTO 28
  ENDIF
28  IF (NTOT(I) .LT. 0.0 .OR. SIGMA .LT. 3.0) THEN
    NTOT(I) = 0.0
    MTOT(I) = 0.0
    KTOT(I) = 0.0
    GOTO 30
  ENDIF
  MASS(I) = NTOT(I)*H2*AREA/(SUN*1E-4)
  VMASS(I) = MTOT(I)*H2*AREA/(SUN*1E-4)
  V2MASS(I) = KTOT(I)*0.5*H2*AREA/(SUN*1E-4)

C  *** ERRORS ***

  EINT(I) = NTOT(I)*DINT(I)/INT(I)
  EMOM(I) = MTOT(I)*DMOM(I)/MOM(I)
  EKE(I) = KTOT(I)*DKE(I)/KE(I)
  DM(I) = MASS(I)*DINT(I)/INT(I)
  DVM(I) = VMASS(I)*DMOM(I)/MOM(I)
  DV2M(I) = V2MASS(I)*DKE(I)/KE(I)

30  CONTINUE

  WRITE (*,*) ' '
  WRITE (*,*) ' *****'
  WRITE (*,*) ' ***** COLUMN DENSITIES *****'
  WRITE (*,*) ' *****'
  WRITE (*,*) ' '
  WRITE (*,*) ' VELOCITY RANGE          N(12CO)
*   (V-V0)N(CO)'
  DO 35 I = 1, II
    WRITE (*,825) VEL1(I),VEL2(I),NTOT(I),'+-',EINT(I),MTOT(I),
*   '+-',EMOM(I)
35  CONTINUE

```

```

WRITE (*,*) ' '
WRITE (*,*) 'VELOCITY RANGE      (V-Vo) N(CO)'
DO 36 I = 1, II
  WRITE (*,826) VEL1(I),VEL2(I),KTOT(I),'+',EKE(I)
36 CONTINUE

WRITE (*,*) ' '
WRITE (*,*) '*****'
WRITE (*,*) '***** MASS CALCULATIONS *****'
WRITE (*,*) '*****'
WRITE (*,*) ' '
WRITE (*,*) 'VELOCITY RANGE      M(H2)
*   (V-Vo)M(H2)'
DO 37 I = 1, II
  WRITE (*,825) VEL1(I),VEL2(I),MASS(I),'+',DM(I),VMASS(I),
*   '+-',DVM(I)
37 CONTINUE
WRITE (*,*) ' '
WRITE (*,*) 'VELOCITY RANGE      (V-Vo) M(H2)'
DO 38 I = 1, II
  WRITE (*,826) VEL1(I),VEL2(I),V2MASS(I),'+',DV2M(I)
38 CONTINUE

DO 40 I = 1, II
  SIGMA = ABS(INT(I)/DINT(I))
  IF (NTOT(I) .LE. 0.0 .OR. SIGMA .LT. 3.0) GOTO 40
  CENTVEL = (VEL1(I) + VEL2(I))/2
  IF (CENTVEL .LT. -7.5 .AND. CENTVEL .GT. -16.5) GOTO 40
  IF (KTOT(I) .LT. 0.0) KTOT(I) = 0.0
  IF (CENTVEL .LT. -16.5) THEN
    NBLUE = NBLUE + NTOT(I)/1E-4
    MBLUE = MBLUE + MTOT(I)/1E-4
    KBLUE = KBLUE + KTOT(I)/1E-4
    BLUM = BLUM + MASS(I)
    BLUVM = BLUVM + VMASS(I)
    BLUV2M = BLUV2M + V2MASS(I)
  ENDIF
  IF (CENTVEL .GT. -7.5) THEN
    NRED = NRED + NTOT(I)/1E-4
    MRED = MRED + MTOT(I)/1E-4
    KRED = KRED + KTOT(I)/1E-4
    REDM = REDM + MASS(I)
    REDVM = REDVM + VMASS(I)
    REDV2M = REDV2M + V2MASS(I)
  ENDIF

  NH2 = NH2 + NTOT(I)/1E-4
  INTERR = INTERR + EINT(I)**2
  MH2 = MH2 + ABS(MTOT(I)/1E-4)
  MOMERR = MOMERR + EMOM(I)**2
  KH2 = KH2 + KTOT(I)/1E-4
  KEERR = KEERR + EKE(I)**2
  MT = MT + MASS(I)

```

```

DMT = DMT + DM(I)**2
VMT = VMT + ABS(VMASS(I))
DVMT = DVMT + DVM(I)**2
V2MT = V2MT + V2MASS(I)
DV2MT = DV2MT + DV2M(I)**2
40 CONTINUE

INTERR = SQRT(INTERR)/1E-4
MOMERR = SQRT(MOMERR)/1E-4
KEERR = SQRT(KEERR)/1E-4
DMT = SQRT(DMT)
DVMT = SQRT(DVMT)
DV2MT = SQRT(DV2MT)

WRITE (*,*) ''
IF (YN .EQ. 'Y') THEN
  * WRITE (*,*) '      N(H2 THIN)      (V-Vo)N(H2 THIN)'
    (V-Vo) M(H2 THIN)'
    WRITE (*,824) 'BLUE ', NBLUE, MBLUE, KBLUE
    WRITE (*,824) 'RED ', NRED, MRED, KRED
    WRITE (*,823) 'TOTAL',NH2,'+-',INTERR,MH2,'+-',MOMERR,KH2,'+-
',KEERR
  ELSE
  * WRITE (*,*) '      N(H2 THICK)      (V-Vo)N(H2 THICK)'
    (V-Vo) M(H2 THICK)'
    WRITE (*,824) 'BLUE ', NBLUE, MBLUE, KBLUE
    WRITE (*,824) 'RED ', NRED, MRED, KRED
    WRITE (*,823) 'TOTAL',NH2,'+-',INTERR,MH2,'+-',MOMERR,KH2,'+-
',KEERR
  ENDIF
  * WRITE (*,*) ''
    WRITE (*,*) '      M(H2)      (V-Vo)M(H2)'
    (V-Vo) M(H2)'
    WRITE (*,824) 'BLUE ', BLUM, BLUVM, BLUV2M
    WRITE (*,824) 'RED ', REDM, REDVM, REDV2M
    WRITE (*,823) 'TOTAL',MT,'+-',DMT,VMT,'+-',DVMT,V2MT,'+-',DV2MT
    AREA = AREA/3.086E18**2
    WRITE (*,*) ''
    WRITE (*,*) ' AREA (pc2) =',AREA
    WRITE (*,*) ''
    WRITE (*,*) ''

800 FORMAT (F7.1,F8.1,F11.3,F8.3,F12.3,F9.3,F13.3,F11.3)
810 FORMAT (F7.1,F8.1,E14.3,E14.3,E14.3)
820 FORMAT (' EXCITATION TEMP. T(EX) =', F8.3)
821 FORMAT (A27,E12.3,A4,E11.3)
822 FORMAT (A32,E12.3,A4,E11.3)
823 FORMAT (A6,E12.3,A3,E10.3,E12.3,A3,E10.3,E12.3,A3,E10.3)
824 FORMAT (A6,E19.3,E25.3,E25.3)
825 FORMAT (F7.1,F8.1,E14.3,A3,E10.3,E14.3,A3,E11.3)
826 FORMAT (F7.1,F8.1,E14.3,A3,E10.3)

STOP
END

```

Curriculum Vitae

Name: Jason W. Schella

Birthplace: Moncton, New Brunswick

Birthday: Nov. 16, 1967

Education: Saint Mary's University, Halifax, Nova Scotia
B.Sc. 1989

Saint Mary's University, Halifax, Nova Scotia
M.Sc. 1991
"A CO J = 2→1 Study of the Outflow Sources GL 490 and NGC
7538 IRS 9"